

Wannier orbital theory and angle-resolved photoemission spectroscopy for the quasi-one-dimensional conductor $\text{LiMo}_6\text{O}_{17}$. II. Intensity variations and the six t_{2g} bands

L. Dudy 

Randall Laboratory, University of Michigan, Ann Arbor, Michigan 48109, USA;
Physikalisches Institut und Röntgen Center for Complex Material Systems, Universität Würzburg, D-97074 Würzburg, Germany;
and Synchrotron SOLEIL, L'Orme des Merisiers, 91190 Saint-Aubin, France

J. W. Allen

Randall Laboratory, University of Michigan, Ann Arbor, Michigan 48109, USA

J. D. Denlinger

Advanced Light Source, Lawrence Berkeley National Laboratory, Berkeley, California 94720, USA

J. He*

Department of Physics and Astronomy, Clemson University, Clemson, South Carolina 29534, USA

M. Greenblatt

Department of Chemistry & Chemical Biology, Rutgers University, 123 Bevier Rd. Piscataway, New Jersey 08854, USA

M. W. Haverkort

Max-Planck-Institut für Festkörperforschung, Heisenbergstrasse 1, D-70569 Stuttgart, Germany;
Max-Planck-Institut für Chemische Physik fester Stoffe, Nöthnitzer Str. 40, D-01187 Dresden, Germany;
and Institut für Theoretische Physik, Universität Heidelberg, Philosophenweg 16, D-69120 Heidelberg, Germany

Y. Nohara and O. K. Andersen

Max-Planck-Institut für Festkörperforschung, Heisenbergstrasse 1, D-70569 Stuttgart, Germany



(Received 27 March 2023; revised 21 November 2023; accepted 27 November 2023; published 21 March 2024)

This is the second paper of a series of three papers presenting a combined study by band theory and angle-resolved photoemission spectroscopy (ARPES) of lithium purple bronze. The t_{2g} Wannier orbitals (WOs) and resulting six-band tight-binding (TB) Hamiltonian found in paper I are used here to develop a theory of the ARPES intensity variations, including a selection rule whose validity relies on the smallness of and the cancellation between the displacement- and inversion-dimerizations of the zigzag chains (ribbons) in regions of the final-state wave vector κ . We then present the ARPES results for the band structure of the four occupied t_{2g} bands (gapped xz , yz , and split metallic xy). A detailed comparison to the theory validates the selection rule. We present the Fermi surface as seen directly in the raw ARPES data, both parallel and perpendicular (using photon-energy dependence) to the sample surface, and show that the selection rule can enable separation of the barely split and highly quasi-one-dimensional xy bands. We adjust the energy of the xy WO energy by 0.1 eV ($\approx 1/4$ of the gap) with respect to that of the gapped xz and yz WOs and, in a second step, fine-tune merely seven out of the more than 40 TB parameters to achieve an excellent fit to the ARPES bands lying more than 0.15 eV below the Fermi level. So doing then also gives nearly perfect agreement closer to the Fermi level.

DOI: [10.1103/PhysRevB.109.115144](https://doi.org/10.1103/PhysRevB.109.115144)

I. INTRODUCTION

This is the second paper in a series of three presenting a detailed study of the band structure of the quasi-one-dimensional (quasi-1D) lithium purple bronze (LiPB) combining the local density approximation N th-order muffin-tin orbital (LDA-NMTO) band theory and angle-resolved photoemission spectroscopy (ARPES).

In paper I [1] we explained the NMTO method (Sec. II) and used it to derive, for the occupied and lowest unoccupied bands of LiPB (Sec. IV), a chemically meaningful set of Wannier functions (Sec. V)—called Wannier orbitals (WO)—and their tight-binding (TB) Hamiltonian in portable, i.e., analytical, form (Sec. VI).

The monoclinic crystal structure of $\text{LiMo}_6\text{O}_{17}$ (Sec. III of paper I) consists of MoO_6 octahedra connected by corners into slabs perpendicular to the reciprocal-lattice vector \mathbf{a}^* . Each slab consists of *bi-ribbons*, four molyb-

*Deceased.

denums wide in the $\mathbf{a} + \mathbf{c}$ direction, $\text{Mo}^2 \setminus \text{Mo}^1 / \text{Mo}^4 \setminus \text{Mo}^5$ and $\text{MO}^5 \setminus \text{MO}^4 / \text{MO}^1 \setminus \text{MO}^2$ [using lowercase/uppercase letters for the lower/upper *string*], and extending indefinitely along the direction \mathbf{b} of quasi-1D conductivity [See Fig. I 2 together with Charts I (14) and (15)].¹ The *spines* of the ribbons are the well-known $\text{Mo}^1 / \text{Mo}^4 \setminus \text{Mo}^1 / \text{Mo}^4$ and $\text{MO}^4 / \text{MO}^1 \setminus \text{MO}^4 / \text{MO}^1$ *zigzag chains* along \mathbf{b} . The upper string is related to the lower by translation of Mo1 to MO1 by the vector $(\mathbf{c} + \mathbf{b})/2 - \mathbf{d}$, followed by *inversion* around their midpoint, $\frac{1}{2}[(\mathbf{c} + \mathbf{b})/2 - \mathbf{d}]$. Had there been *no* displacement ($\mathbf{d} = 0$) and *no* inversion, i.e., no *c*-axis dimerization (Sec. I III A), all ribbons would have been related by a primitive translation vector $(\mathbf{c} + \mathbf{b})/2$, and thus stacked into a ramp [Chart I (21)]. *With* displacement and inversion dimerizations, the slab forms a *staircase* [Chart I (14)] with steps of bi-ribbons and running up and down along $\pm \mathbf{c}$. A staircase is terminated by insulating MoO_4 tetrahedra, and Li intercalates between staircases which is also where the crystal cleaves.

We found that the six lowest-energy bands (Figs. I 3 and I 4)—half occupied—are accurately described by the set of six, real-valued t_{2g} WOs,¹⁴ $w_m = xy, xz, yz$ centered on Mo1, and $W_m = XY, XZ, YZ$, centered on MO1, and with x, y , and z directions as indicated in Charts I (14) and I (15). Such a t_{2g} WO has tails with the same m on the nearest Mo neighbors in its plane which contribute to the halo of the WO (Figs. I 5 and I 9).

The xy WOs lie well inside their respective ribbon and have strong, long-ranged $dd\pi$ xy - xy or XY - XY hopping integrals τ_n , with Bloch sum $\tau(k_b)$ along the ribbon, very weak $dd\delta$ xy - XY hopping integrals $t_n + u_n$ between partner ribbons, and even weaker hopping integrals $t_n - u_n$ between bi-ribbons [Eqs. I (36), I (37), I (43), and I (44)]. Between slabs, the hopping is negligible. The xz and yz WOs, which are equivalent, stand perpendicular to the ribbons and the $dd\pi$ nearest-neighbor hopping integral $A_1 + G_1$, between partner ribbons—up or down the staircase with steps $(\mathbf{c} - \mathbf{b})/2$ for xz - XZ and $(\mathbf{c} + \mathbf{b})/2$ for yz - YZ —is twice as strong as the hopping integral $A_1 - G_1$ between bi-ribbons. The two xz bands are gapped by the hopping dimerization, $\pm 2G_1 \approx \mp 0.2$ eV, and so are the two yz bands [Eqs. I (38) and I (45)].

In our notation, greek-lettered Bloch sums, e.g., τ , are over hops on the ribbon, whereby they are real and single-zone periodic in \mathbf{k} . Latin-lettered Bloch sums, such as t, u, A , and G , are over hops *between* ribbons and are therefore real and double-zone periodic [Eqs. I (41) and I (42)].

In Eq. I (35) we gave the *six-band TB Hamiltonian* in the representation of the Bloch-summed WOs, $w_m(\mathbf{r}, \mathbf{k}) \equiv \sum_{\mathbf{T}} e^{2\pi i \mathbf{k} \cdot \mathbf{T}} w_m(\mathbf{r} - \mathbf{T})$ and $W_m(\mathbf{r}, \mathbf{k}) \equiv \sum_{\mathbf{T}} e^{2\pi i \mathbf{k} \cdot \mathbf{T}} W_m(\mathbf{r} - \mathbf{T})$, with the latter multiplied by $e^{2\pi i \mathbf{k} \cdot (\mathbf{c} + \mathbf{b})/2} = e^{\pi i (k_c + k_b)}$ so that the *hopping dimerizations are purely imaginary*; numerically, they are about 30% of the corresponding hopping integral. Further insight was gained by transforming from this sublattice $\{w, W\}$ representation (Sec. I VI A) to the reciprocal sublattice $\{\mathbf{k}, \mathbf{k} + \mathbf{c}^*\}$ representation (Sec. I VI B), i.e., from

a basis with two sets of Bloch sums $w_m(\mathbf{r}, \mathbf{k})$ and $W_m(\mathbf{r}, \mathbf{k})$, each a periodic function of \mathbf{k} in the single zone, to a set of *pseudo* Bloch sums,

$$\left| m; \begin{array}{c} \mathbf{k} \\ \mathbf{k} + \mathbf{c}^* \end{array} \right\rangle = \frac{1}{\sqrt{2}} \sum_{\mathbf{T}} e^{2\pi i \mathbf{k} \cdot \mathbf{T}} \left[w_m(\mathbf{r} - \mathbf{T}) \pm e^{\pi i (k_c + k_b)} W_m(\mathbf{r} - \mathbf{T}) \right] \quad \text{I (52),}$$

which are periodic functions of \mathbf{k} in the *double zone* (Fig. I 8, repeated here as Fig. II 1) and evaluated in two different single zones, i.e. at \mathbf{k} and $\mathbf{k} + \mathbf{c}^*$. Each pseudo-Bloch sum is over *both* ribbons with the phase factor multiplying $W(\mathbf{r} - \mathbf{T})$ chosen as if there were *no* displacement dimerization, \mathbf{d} [see Eqs. I (17) and I (18)], i.e., as $e^{2\pi i \mathbf{k} \cdot (\mathbf{c} + \mathbf{b})/2}$. In this representation, the six-band Hamiltonian is I (56). It is now conceivable that *the ARPES intensity* from an occupied band follows its $|\mathbf{k}|$ character, i.e., what we called its *fatness* in Sec. I VI C and showed in Fig. I 10 for the two xy bands at $k_b = 0.225$ and as functions of k_c . In the absence of dimerization, the two pseudo Bloch sums are linearly dependent, and the $|\mathbf{k}|$ - and $|\mathbf{k} + \mathbf{c}^*|$ -projected bands are double-zone periodic and translated by \mathbf{c}^* with respect to each other. *With* dimerization, the pseudo Bloch sums become linearly *independent* and mix near the crossings of the undimerized \mathbf{k} and $(\mathbf{k} + \mathbf{c}^*)$ bands, where the dimerized bands will gap and thus restore the single-zone periodicity. Correspondingly, the $|\mathbf{k}|$ projection follows the undimerized \mathbf{k} band except near its crossing with the undimerized $(\mathbf{k} + \mathbf{c}^*)$ band, where it loses half its intensity to the $|\mathbf{k} + \mathbf{c}^*|$ -projected band (see Fig. I 6).

The first task of the present paper II is to derive an expression for the variation of ARPES intensity with \mathbf{k} which *includes* its *distortion* caused by *c*-axis displacement and inversion dimerizations. To do so, we neglect the coupling between t_{2g} WOs with different m , a good approximation near the FS ($|k_b| \approx 1/4$), and in fact everywhere, except near the Γ Z-line ($k_b = 0$). In this *pure-m*-band approximation introduced in Sec. I VI C, the six-band Hamiltonian factorizes in three 2×2 Hamiltonians H_m with eigenvalues

$$\pm \sqrt{A^2 + G^2}, \quad \pm \sqrt{\bar{A}^2 + \bar{G}^2}, \quad \text{and} \quad \tau \pm \sqrt{t^2 + u^2}, \quad \text{I (57)}$$

for $m = xz, yz$, or xy , respectively, and with \mathbf{k} dependencies given by Eqs. I (38), I (37), and I (36). The crossings I (32), I (31), and I (30) of these *pure-m* bands define the boundaries of the so-called *physical zones* shown in Fig. 1. The eigenfunctions of the *pure-m* bands were given by

$$w_1^{\pm}(\mathbf{k}, \mathbf{r}) = \frac{1}{\sqrt{2}} \left[w(\mathbf{k}, \mathbf{r}) e^{-i\phi(\mathbf{k})} \mp W(\mathbf{k}, \mathbf{r}) e^{\pi i (k_c + k_b)} \right] \quad \text{I (58)}$$

$$= \frac{1}{2} \left[|w; \mathbf{k}\rangle (e^{-i\phi(\mathbf{k})} \mp 1) \pm |w; \mathbf{k} + \mathbf{c}^*\rangle (e^{-i\phi(\mathbf{k})} \pm 1) \right], \quad \text{I (59)}$$

where the *band-structure phase* $\phi(\mathbf{k})$ is the phase of the complex Bloch-summed inter-ribbon hopping integral whose imaginary part gives the asymmetry between the hopping in and outside the bi-ribbon, i.e., the *initial-state dimerization*:

$$e^{i\phi} \equiv \frac{-A - iG}{\sqrt{A^2 + G^2}}, \quad \frac{-\bar{A} - i\bar{G}}{\sqrt{\bar{A}^2 + \bar{G}^2}}, \quad \text{and} \quad \frac{-t - iu}{\sqrt{t^2 + u^2}}. \quad \text{I (60)}$$

For quasi-1D structures, the band-structure phase $\phi(\mathbf{k})$ varies from zero for \mathbf{k} at the center of the physical zone to $+\frac{\pi}{2}$ ($-\frac{\pi}{2}$)

¹I, II, and III refer to sections, figures, equations, and footnotes in papers I [1], II, and III [2], respectively.

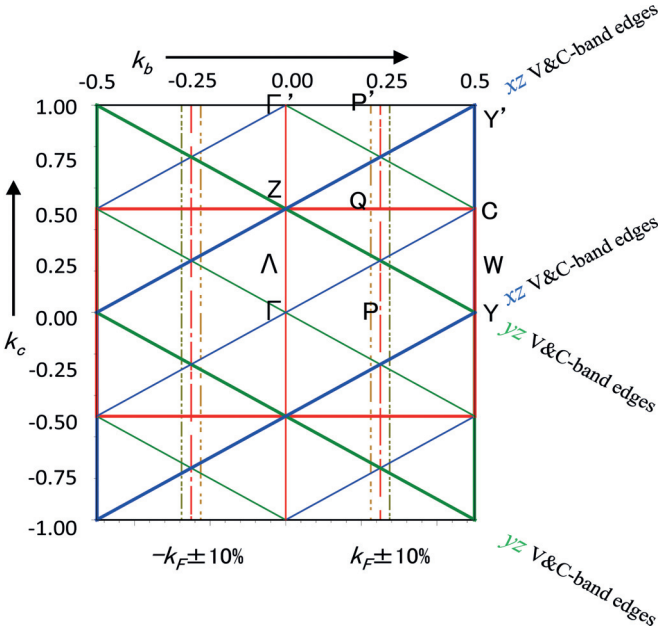


FIG. 1. Double zone, same as Fig. 8 in paper I. The first (second) physical zones shown in solid lines for the xy (red), xz (blue), and yz (green) pure bands are, respectively, $|k_c| \leq \frac{1}{2}$, $|k_c + k_b| \leq \frac{1}{2}$, and $|k_c - k_b| \leq \frac{1}{2}$. The red zone is the BZ, and its irreducible part is the one with $0 \leq k_c \leq 0.5$. Weak lines indicate the positions of pure-band maxima and minima (see Fig. I 6). The red dot-dashed lines indicate the positions of the left and the right, doubly degenerate Fermi-surface sheets for stoichiometric $2(\text{LiMo}_6\text{O}_{17})$. The brown and olive dot-dashed lines respectively correspond to 10% hole and electron doping. See Sec. I IV A and Sec. III D. The figure is to scale because the triangles are almost equilateral.

at right (left) zone boundaries (ZBs), and to $\pm\pi$ at the centers of the second zones.

According to Eq. I (59), the $|\mathbf{k}$ character [fatness, $f_2(\mathbf{k})$] of the upper (lower) m band illustrated in Fig. I 10 is $[1 \mp \cos \phi_m(\mathbf{k})]/2$. In Sec. II B 1, we shall show that the intensity of photoemission from the upper (lower) m band is simply $[1 \mp \cos\{\phi_m(\mathbf{k}) - \eta_m(\kappa)\}]/2$, which means that the band-structure phase is shifted by $\eta_m(\kappa)$, the phase shift (9) experienced by an electron emitted with momentum κ and caused by the c -axis inversion- and displacement dimerizations (see Sec. I III A). This phase shift *distorts* the switching curves in Fig. I 10 to what is shown in the middle panel of Fig. 2.

On top of these *fine-grained* intensity variations caused by the near-translational equivalence Eq. I (17) of the WOs on the upper and lower ribbons, there are *coarse-grained* variations due to the approximate translational equivalence Eq. I (12) of the tails on the Mo neighbors in the plane of the WO (see Fig. I 5) and therefore described by the WO form factor (Sec. II B 2).

The understanding of the ARPES intensity variations gained in Sec. II enabled us to obtain the new, detailed ARPES results for the occupied part of the t_{2g} bands which we present in Sec. III, compare with the WO band theory (Secs. III D and III E), and in Sec. IV use to adjust the parameters of the six-band TB Hamiltonian presented in Sec. VI of paper I [1]. Important information on the technical experimental details

are given in Secs. III A and III B. The ARPES FS measurements turned out to have a rather strong photon-energy dependence (Sec. III C) whose origin seems to be the narrowness along κ_c of the form factor for the $\tilde{x}y$ WO, i.e., the widening along \mathbf{c} of $w_{\tilde{x}y}(\mathbf{r})$ caused by the hybridization with the valence band (see Sec. II A in paper III).

II. THEORY OF ARPES INTENSITY VARIATIONS IN LiPB

Our ARPES data to be presented in Sec. III show (fine-grained) intensity variations between equivalent zones, similar to the BZ-selection effects observed in graphite and explained by Shirley *et al.* [3]. The primitive cell of LiPB, $\text{Li}_2\text{Mo}_{12}\text{O}_{34}$, is, however, much larger than that of graphite, C_2 , and its ARPES intensity exhibits not only fine-grained zone selection but also coarse-grained structures in reciprocal space. On the other hand, like in graphite, there are only four occupied bands in LiPB, and this together with the reduction of the dimensionality from two dimensions (2D) to quasi-1D enables a simple description for LiPB in terms of WOs. As we explain, it is the tails of the Mo1 and Mo1-centered t_{2g} WOs, $w_m(\mathbf{r})$ and $W_m(\mathbf{r})$ seen in Fig. I 9, which give rise to the coarse-grained structure,² and it is the approximate equivalence I (17) by half a lattice translation which gives rise to the fine-grained structure. This zone-selection effect is simpler than the one found for the π band in graphite because it is due to the existence of a hypothetical, undimerized form [$\text{LiMo}_6\text{O}_{17}$ in Charts I (21) and (22)] of LiPB, which cannot exist for C_2 where the two carbons are far from being separated by half a lattice vector.

A. Preliminaries

We first follow the treatment of Shirley *et al.* [3], but in the next section switch from their representation of the initial states in terms of atomic orbitals (AOs) to one in terms of WOs. Hence, we start from the one-step (Fermi's golden rule) expression:

$$I(\kappa, \omega) \propto \theta(\omega) \sum_{j\mathbf{k}}^{\text{zone}} \delta[E_j(\mathbf{k}) + \omega] \times |e^{2\pi i \kappa \cdot \mathbf{r}} |\mathbf{p} \cdot \mathbf{E}| \psi_j(\mathbf{k}, \mathbf{r})|^2, \quad (1)$$

for the photoemission intensity as functions of the electrons binding energy ω and momentum $(2\pi)\kappa$ inside the sample. Surface effects are neglected. We have used the one-electron approximation with initial-state Bloch functions $\psi_j(\mathbf{k}, \mathbf{r})$ and energy bands $E_j(\mathbf{k})$ with respect to the Fermi level. The sum in (1) is over all occupied states $j\mathbf{k}$ with \mathbf{k} in a (single) zone and $\sum_{\mathbf{k}}$ denoting the average over this zone. For simplicity—and lack of knowledge—the final state inside the sample is taken as the plane wave $e^{2\pi i \kappa \cdot \mathbf{r}}$, the least specific choice possible. For our purpose, it suffices to express the matrix element as

$$\langle e^{2\pi i \kappa \cdot \mathbf{r}} |\mathbf{p} \cdot \mathbf{E}| \psi_j(\mathbf{k}, \mathbf{r}) \rangle \propto (\kappa \cdot \hat{\mathbf{e}}) \langle e^{2\pi i \kappa \cdot \mathbf{r}} | \psi_j(\mathbf{k}, \mathbf{r}) \rangle \quad (2)$$

²This effect is not included in the recent *Experimentalist's Guide to the Matrix Element in ARPES* [4] because the WOs used there did not extend over several atoms per primitive cell.

as obtained by, first of all, operating with the dipole operator $\mathbf{p} \cdot \mathbf{E}$ to the left, that is on the plane wave, and then by pulling the polarization-dependent factor from Eq. (23) outside the integral, exploiting the fact that the photon wavelength is long compared with interatomic distances. The proportionality constants in (1) and (2) are independent of the initial states.

Hence, photoemission at energy ω occurs for κ at the constant-energy contours $\omega = -E_j(\kappa[\text{mod zone}])$ with an intensity which, contrary to $E_j(\mathbf{k})$, is aperiodic in the reciprocal lattice and depends on the polarization of the photons and on the initial states $\psi_j(\mathbf{k}, \mathbf{r})$ of the electrons.

The initial states may be expanded in Bloch sums I (8) of localized orbitals $\chi_{RL}(\mathbf{r})$, e.g., AOs, NMTOs, or WOs:

$$\begin{aligned} \psi_j(\mathbf{k}, \mathbf{r}) &= \sum_{RL}^{\text{cell}} \chi_{RL}(\mathbf{k}, \mathbf{r}) u_{RL,j}(\mathbf{k}) \\ &= \sum_{RL}^{\text{cell}} \sum_{\mathbf{T}} \chi_{RL}(\mathbf{r} - \mathbf{T}) e^{2\pi i \mathbf{k} \cdot \mathbf{T}} u_{RL,j}(\mathbf{k}). \end{aligned} \quad (3)$$

Since for a Bloch sum I (8) of orbitals, $\chi_R(\mathbf{r})$ centered¹⁴ at $\mathbf{r} = \mathbf{R}$,

$$\begin{aligned} \langle e^{2\pi i \mathbf{k} \cdot \mathbf{r}} | \chi_R(\mathbf{k}, \mathbf{r}) \rangle &= e^{-2\pi i \mathbf{k} \cdot \mathbf{R}} \int \chi_R(\mathbf{r}) e^{-2\pi i \mathbf{k} \cdot (\mathbf{r} - \mathbf{R})} d^3 r \sum_{\mathbf{T}} e^{-2\pi i (\mathbf{k} - \mathbf{k}) \cdot \mathbf{T}} \\ &= e^{-2\pi i \mathbf{k} \cdot \mathbf{R}} \tilde{\chi}_R(\kappa) \sum_{\mathbf{G}} \delta(\kappa - \mathbf{k} - \mathbf{G}), \end{aligned} \quad (4)$$

where the sum is over all points \mathbf{G} of the reciprocal lattice and

$$\tilde{\chi}_R(\kappa) \equiv \int \chi_R(\mathbf{r}) e^{-2\pi i \mathbf{k} \cdot (\mathbf{r} - \mathbf{R})} d^3 r \quad (5)$$

is the Fourier transform (FT)³ of $\chi_R(\mathbf{r})$. Note that we use a notation according to which real-space functions such as $\chi_R(\mathbf{r})$ are centered at $r = R$, but their Fourier transforms, $\tilde{\chi}_R(\kappa)$, defined by (5), only depend on their shape and not on where they are centered.

The second factor of the matrix element (2) thus factorizes as

$$\begin{aligned} \langle e^{2\pi i \mathbf{k} \cdot \mathbf{r}} | \psi_j(\mathbf{k}, \mathbf{r}) \rangle &= \sum_{RL}^{\text{cell}} e^{-2\pi i \mathbf{k} \cdot \mathbf{R}} \tilde{\chi}_{RL}(\kappa) u_{RL,j}(\mathbf{k}) \\ &\quad \times \sum_{\mathbf{G}} \delta(\kappa - \mathbf{k} - \mathbf{G}), \end{aligned}$$

whereby expression (1) for the photoemission intensity becomes

$$\begin{aligned} I(\kappa, \omega) &\propto (\kappa \cdot \hat{\mathbf{e}})^2 \theta(\omega) \sum_{j\mathbf{k}}^{\text{zone}} \delta[E_j(\mathbf{k}) + \omega] \\ &\quad \times \left| \sum_{RL}^{\text{cell}} e^{-2\pi i \mathbf{k} \cdot \mathbf{R}} \tilde{\chi}_{RL}(\kappa) u_{RL,j}(\mathbf{k}) \sum_{\mathbf{G}} \delta(\kappa - \mathbf{k} - \mathbf{G}) \right|^2, \end{aligned} \quad (6)$$

³The small tilde denoting the FT has nothing to do with the large tilde denoting the downfolding of the xz and yz characters into the $\tilde{x}\tilde{y}$ states in the gap.

which vanishes unless the wave vector κ of the final electronic state inside the sample (see Sec. III A) equals the Bloch vector \mathbf{k} of the initial electronic state, plus an arbitrary reciprocal-lattice vector \mathbf{G} . In (6), $\sum_{\mathbf{G}}$ is a periodic function of $\kappa - \mathbf{k}$ in the \mathbf{G} lattice, but the other factors are not.

An AO factorizes as $\chi_{RL}(\mathbf{r}) \equiv Y_L(\hat{\mathbf{r}}_R) \varphi_{RL}(r_R)$, whereby its FT (5), which depends on its shape L , including its orientation, but *not* on its center \mathbf{R} , can be taken outside the sum over translationally equivalent AOs:

$$\begin{aligned} \sum_{R \in \text{eq}}^{\text{cell}} e^{-2\pi i \mathbf{k} \cdot \mathbf{R}} \tilde{\chi}_{RL}(\kappa) u_{RL,j}(\mathbf{k}) &= \tilde{Y}_L(\hat{\kappa}) \int j_L(2\pi \kappa r) \varphi_{RL}(r) r^2 dr \sum_{R \in \text{eq}}^{\text{cell}} e^{-2\pi i \mathbf{k} \cdot \mathbf{R}} u_{RL,j}(\mathbf{k}), \end{aligned} \quad (7)$$

thus leaving the sums $\sum_{R \in \text{eq}}^{\text{cell}}$ over the translationally inequivalent AOs to be performed later. Hence, the sum (7) over translationally equivalent AOs factorizes into a κ -dependent AO form factor, times a so-called (Refs. [5–7]) photoemission structure factor (PSF). The latter is similar to the geometrical structure factor in x-ray diffraction but depends on the initial-state wave function [via its linear combination of atomic orbitals (LCAO) coefficients $u_{RL,j}(\mathbf{k})$]. This factorization holds for the π band in C_2 because this band is singly degenerate and contains only one type of orbital, $Y_{10} = p_z$, so that the entire sum, $\sum_{RL}^{\text{cell}} e^{-2\pi i \mathbf{k} \cdot \mathbf{R}} \tilde{\chi}_{RL}(\kappa) u_{RL,j}(\mathbf{k})$, reduces to the factorized form (7). The PSF for the graphene π band thus depends merely on the \mathbf{k} -dependent phase between the p_z orbitals on the two atoms [3]. However, to the three σ bands in graphene, *three* translationally inequivalent AOs on each of the two C atoms (s , p_x , and p_y , or the three equivalent sp^2 orbitals directed toward the three nearest neighbors) contribute, so that, for the σ bands, $\sum_{RL}^{\text{cell}} e^{-2\pi i \mathbf{k} \cdot \mathbf{R}} \tilde{\chi}_{RL}(\kappa) u_{RL,j}(\mathbf{k})$ does *not* factorize into an orbital form factor and a geometrical structure factor.

Whereas eight AOs are needed to describe the occupied bands in graphene, LiPB needs more than 300 atomically localized AOs (see Sec. I II) but, by virtue of its quasi-1D structure, needs merely the six t_{2g} WOs shown in Fig. I 9. Using those in expression (6) for the ARPES intensity and neglecting inter- m mixing leads to great simplification, as we shall now see.

B. Using the six t_{2g} Wannier orbitals

For LiPB, we predict, and in Sec. III E confirm, that the near-translational equivalence of the t_{2g} WOs $w_m(\mathbf{r})$ and $W_m(\mathbf{r})$ by half a lattice translation causes the ARPES to have double-period fine-grained intensity variations which approximately follow the $|\mathbf{k}|$ character I (61), shown as fatness in Figs. I 6, I 7, and I 10, of the occupied bands. This implies that the m band with the lower energy appears in the first physical zone and is extinguished near the center of the second physical zone, and conversely for the m band with higher energy. On top of this comes the fact that the upper xz and yz bands are unoccupied and therefore cause no intensity in their respective second physical zones. The metallic xy band with the lower

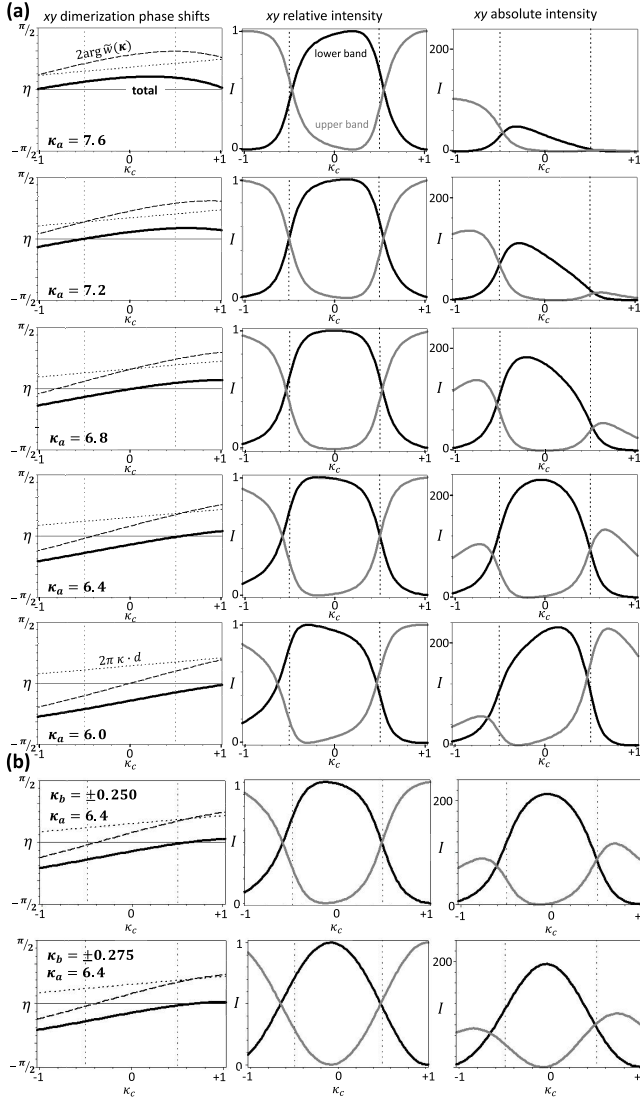


FIG. 2. (a) Photoemission from the xy bands (red in Fig. 4) for $|\kappa_b| = |\kappa_c| = 0.225$ and as functions of $\kappa_c = \kappa_c$ in the double zone, i.e., along a brown dot-dashed line in Fig. 1. See also Fig. I 10. (column 1) Inversion- $[2 \arg \tilde{w}(\kappa)]$, dashed], displacement- $(2\pi \kappa \cdot \mathbf{d})$, dotted), and total- $[\eta(\kappa)]$, full] dimerization phase shift for $\kappa_a = 6.0$ – 7.6 . (column 2) Relative intensities of photoemission, $[1 \mp \cos\{\phi(\mathbf{k}) - \eta(\kappa)\}]/2$, from the upper (light) and lower (dark) bands. These intensities exhibit the fine-grained structure. (column 3) Absolute photoemission intensities, i.e., the relative intensities in column 2 times the polarization- and WO form factors $(\kappa \cdot \hat{\mathbf{e}})^2 |\tilde{w}(\kappa)|^2$ evaluated in Sec. II B 2 and shown in the top panel of Fig. 4. These polarization and WO form factors provide the coarse-grained structure. (b) Same as panel (a) but along $|\kappa_b| = |\kappa_c| = 0.250$, a red dot-dashed line in Fig. 1 (top), and along $|\kappa_b| = |\kappa_c| = 0.275$, an olive dot-dashed line (bottom), and only for $\kappa_a = 6.4$. The boundaries of the first zone are indicated by vertical, dotted lines.

energy should best be seen in the 1st BZ and the xy band with the higher energy in the 2nd BZ. This zone-selection effect will allow us to resolve the perpendicular dispersion and splitting of the quasi-1D $\tilde{x}\tilde{y}$ bands predicted in the bottom panel of Fig. 4. We shall see that the deviations from the

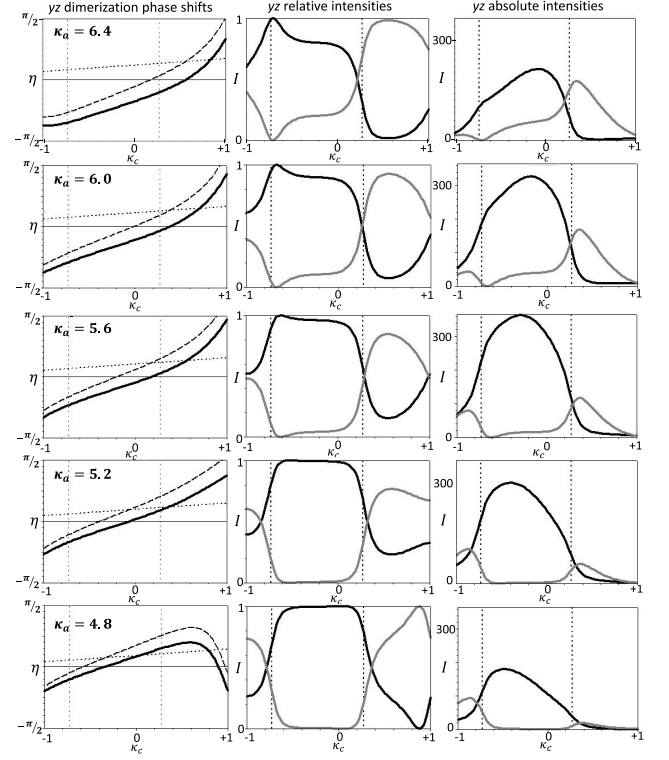


FIG. 3. Same as in Fig. 2, but for the yz bands (green in Fig. 4) and for $\kappa_a = 4.8$ – 6.4 . The green zone boundaries in Fig. 1 intersect the brown dot-dashed near-FS line, $\kappa_b = 0.225$, at $\kappa_c = 0.275$ and at $0.275 - 1 = -0.725$, which is where the switching curves would have crossed had there been no dimerization distortion, i.e., if $\eta_{yz}(\kappa) = 0$. Since the upper yz band is empty, the light switching curves should have been deleted.

translational equivalence of $w_m(\mathbf{r})$ and $W_m(\mathbf{r})$, i.e., the inversion- and displacement dimerizations expressed after Eq. I (18), will distort the ARPES intensity variation from that of the initial-state $|\mathbf{k}\rangle$ character, $\frac{1}{2}[1 \mp \cos \phi(\mathbf{k})]$, to $\frac{1}{2}[1 \mp \cos\{\phi(\mathbf{k}) - \eta(\kappa)\}]$, where $\eta(\kappa)$ is the dimerization phase shift (9) of the emitted electron with momentum κ . By suitable choice of κ_a , via control of the photon energy [see, e.g., Eq. (27)], this distortion can be negligible for the xy bands in a large part of the double zone and may also be so for the occupied xz and yz bands.

In addition to the *fine-grained zone-selection* effect (Sec. II B 1), well known from the geometrical *structure factor* in x-ray crystallography, we predict (Sec. II B 2) and find (Sec. III) that the *internal* structure of the $w_m(\mathbf{r})t_{2g}$ WO, spreading out to about the four nearest molybdenums in its plane (see Fig. I 5), makes the *form factor of the WO* approximately factorize into a *coarse-grained structure factor*, times the *form factor of the local* partial-wave projection $Y_{2m}(\hat{\mathbf{r}})\varphi_2(r)$ of the WO tail.

1. Zone selection: The fine-grained structure

The DFT calculation resulting in the low-energy six-band t_{2g} TB Hamiltonian and in the band structures in Figs. 10(b) and 12 shows that—except near band crossings such as those below -0.5 eV and those near the top of the valence bands

near Z —each band is dominated by *one* m character. For describing the ARPES matrix elements, but not the bands, we shall neglect by-mixing of WOs with other m values, i.e., use the pure- m approximation (Sec. I VI C). Therefore, in the general expression (3) for the initial-state wave function, L

$$\begin{aligned} \langle e^{2\pi i \mathbf{k} \cdot \mathbf{r}} | w_1(\mathbf{k}, \mathbf{r}) \rangle &= \frac{1}{\sqrt{2}} \sum_{\mathbf{G}} \delta(\boldsymbol{\kappa} - \mathbf{k} - \mathbf{G}) [\tilde{w}(\boldsymbol{\kappa}) e^{-i\phi(\mathbf{k})} \mp \tilde{W}(\boldsymbol{\kappa}) e^{2\pi i \boldsymbol{\kappa} \cdot \mathbf{d}}] \\ &= \frac{1}{\sqrt{2}} \sum_{\mathbf{G}} \delta(\boldsymbol{\kappa} - \mathbf{k} - \mathbf{G}) \tilde{w}(\boldsymbol{\kappa}) [e^{-i\phi(\mathbf{k})} \mp e^{-i\eta(\boldsymbol{\kappa})}]. \end{aligned} \quad (8)$$

For the FTs of $w(\mathbf{k}, \mathbf{r})$ and $W(\mathbf{k}, \mathbf{r})$ we have used Eq. (4) with the sum being over all points \mathbf{G} of the reciprocal lattice.⁴ Inside this sum, the product of the phase factors, $e^{\pi i(k_c + k_b)}$ and $\exp[-2\pi i \boldsymbol{\kappa} \cdot (\frac{\mathbf{c} + \mathbf{b}}{2} - \mathbf{d})]$, from, respectively Eqs. I (58) and (4) is simply $e^{2\pi i \boldsymbol{\kappa} \cdot \mathbf{d}}$ with \mathbf{d} being the displacement dimerization I (16) and $\boldsymbol{\kappa}$ the momentum of the emitted electron. On the second line of Eq. (8) we have used that, due to the inversion dimerization I (18), $\tilde{W}(\boldsymbol{\kappa}) = \tilde{w}(-\boldsymbol{\kappa})$ and that $\tilde{w}(-\boldsymbol{\kappa}) = \tilde{w}(\boldsymbol{\kappa})^* = |\tilde{w}(\boldsymbol{\kappa})| e^{-i \arg \tilde{w}(\boldsymbol{\kappa})}$ because $w(\mathbf{r})$ is a real-valued t_{2g} function. As a consequence, $e^{2\pi i \boldsymbol{\kappa} \cdot \mathbf{d}} \tilde{W}(\boldsymbol{\kappa}) / \tilde{w}(\boldsymbol{\kappa}) = e^{-i\eta(\boldsymbol{\kappa})}$, where

$$\eta_m(\boldsymbol{\kappa}) \equiv 2 \arg \tilde{w}_m(\boldsymbol{\kappa}) - 2\pi \boldsymbol{\kappa} \cdot \mathbf{d} \quad (9)$$

$$\begin{aligned} I(\boldsymbol{\kappa}, \omega) &\propto (\boldsymbol{\kappa} \cdot \hat{\mathbf{e}})^2 \theta(\omega) \sum_{j=1}^2 \sum_{\mathbf{k}}^{\text{zone}} \delta[E_j(\mathbf{k}) - E_F + \omega] \left| \sum_{\mathbf{G}} \delta(\boldsymbol{\kappa} - \mathbf{k} - \mathbf{G}) \tilde{w}(\boldsymbol{\kappa}) [e^{-i\phi(\mathbf{k})} \mp e^{-i\eta(\boldsymbol{\kappa})}] \right|^2 \\ &\propto \sim (\boldsymbol{\kappa} \cdot \hat{\mathbf{e}})^2 |\tilde{w}(\boldsymbol{\kappa})|^2 \theta(\omega) \sum_{j=1}^2 \sum_{\mathbf{k}}^{\text{zone}} \delta[E_j(\mathbf{k}) - E_F + \omega] \delta[\boldsymbol{\kappa} - (6, 0, 0) - \mathbf{k}] \frac{1 \mp \cos[\phi(\mathbf{k}) - \eta(\boldsymbol{\kappa})]}{2}, \end{aligned} \quad (10)$$

where the second line holds when—hinging on the coarse-grained structure of $\tilde{w}(\boldsymbol{\kappa})$ and the experimental setup—the \mathbf{G} sum is *dominated by one term*, the one for $\mathbf{G} = (6, 0, 0)$ in our case, as we shall see in the following section, Figs. 5 and 6 in particular. We can then use that $\frac{1}{4} |e^{-i\phi} \mp e^{-i\eta}|^2 = [1 \mp \cos(\phi - \eta)]/2$, which is like in Eq. I (61) and illustrated in Fig. I 10, but shifted by η , and obtain the simple result that the intensity of photoemission from two dimerized m bands ($j = 1, 2$) in LiPB follows the $|\mathbf{k}|$ character (fatness), but with the band-structure phase $\phi(k_b, k_c)$ [Eq. I (60) in the introduction] *shifted* by the dimerization phase shift $\eta(k_a + 6, k_b, k_c)$. Remembering that ϕ is independent of k_a due to the long paths for hopping between slabs¹⁵ and varies from $-\pi/2$ to $+\pi/2$ across the first zone, we realize that dimerization phase shift shown by the full curves in the first columns of Figs. 2 and 3 can merely *distort* the switching curves, and less so for the xy bands than for the equivalent yz and xz bands.

⁴The reciprocal-lattice points \mathbf{G} and the Bloch sum of hopping integrals G should not be confused.

takes *one* value (m), R takes two values (MO1 and MO1), and expression (3) becomes Eq. I (58), which is repeated in the introduction to the present paper.

Hence, the second factor of the matrix element (2) for photoemission from the upper ($j = 2$) or lower ($j = 1$) m -band state is the FT of the respective eigenfunction I (58):

is the *dimerization phase shift* whose first term is due to the inversion dimerization and the second to the displacement dimerization. The latter, $2\pi(0.012\kappa_a + 0.033\kappa_c)$, is a weak function of κ_c , a very weak function of κ_a , and is independent of κ_b and m . It is the dotted, linear curves shown in the first columns of Figs. 2 and 3. The first term in expression (9), the phase shift due to inversion dimerization, is the dashed curves in the first columns which we have evaluated as will be explained in the next section II B 2 using the rough digitalizations (12) and (13) of Figs. I 5 and I 9.

The intensity (6) of photoemission from two dimerized m bands ($j = 1, 2$) in LiPB is thus

This is seen in the middle panels of Figs. 2 and 3. For the xy bands along the $\kappa_b = 0.225$ line slightly inside the FS, the distortions increase with the deviation of κ_a from the value 6.8. Similarly for switching curves for the yz bands in Fig. 3, the distortions increase with the deviation of κ_a from the value 5.3.

As seen in the first columns of Figs. 2 and 3, the inversion (dash) and displacement (dots) phase shifts *tend to cancel out*: For the xy bands along $\kappa_b = 0.225$, a zero of $\eta(\boldsymbol{\kappa})$ (full) increases through the first xy zone ($-1/2|1/2$) for κ_a decreasing from 7.4 to 6.4, and for the yz bands along the same line, the zero *decreases* through the first yz zone for κ_a decreasing from 5.5 to 4.5. In these intervals of κ_a , the c -axis dimerization hardly distorts the zone selection, as seen in the second column. That the distortions due to displacement and inversion dimerizations tend to cancel over a κ_a region of order 1 for both the xy and yz bands is surprising considering the fact that the $dd\delta$ coupling between the $xy(\mathbf{r})$ and $XY[\mathbf{r} - (\mathbf{c} + \mathbf{b})/2 + \mathbf{d}]$ WOs is much smaller than the $dd\pi$ coupling between $yz(\mathbf{r})$ and $YZ[\mathbf{r} - (\mathbf{c} + \mathbf{b})/2 + \mathbf{d}]$, but for the latter, the distortions are of course larger.

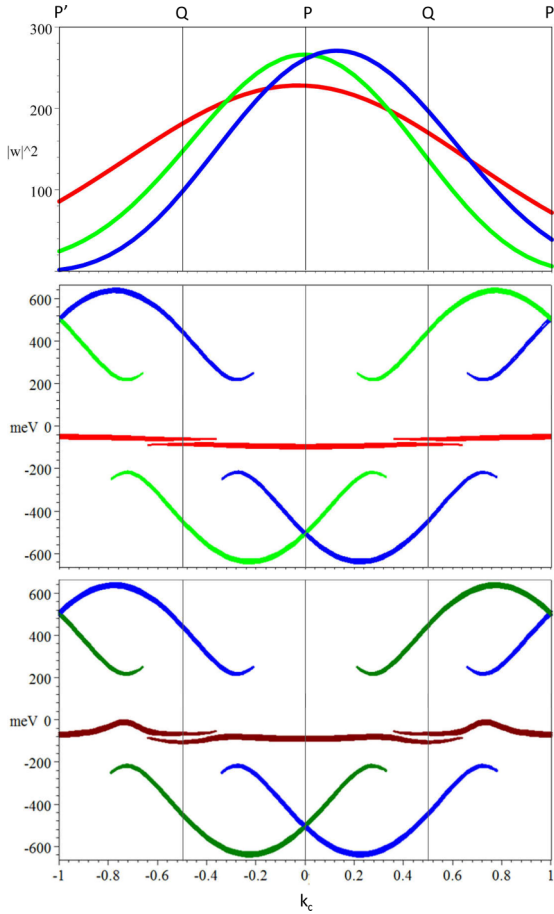


FIG. 4. *Top*: Polarization and form factor intensities $(\boldsymbol{\kappa} \cdot \hat{\mathbf{e}})^2 |\tilde{w}_m(\boldsymbol{\kappa})|^2$ for $m = xy$ (red), xz (blue), and yz (green) along the P'QPQP' line, $\kappa_b = 0.225$, in the double zone $-1 < \kappa_c \leq 1$. These aperiodic coarse-grained intensities depend on κ_a —chosen here to be 6.4—as explained in Sec. III B. (*middle and bottom*) Band-factor intensities according to Eq. (10) without dimerization, i.e., with $\eta_m(\boldsymbol{\kappa}) = 0$. They are the $|\mathbf{k}$ -projected bands [see Eq. I (61)] and give rise to the fine-grained intensity distributions with period two in κ_c . Their dependence on κ_a is negligible. Like in Figs. I 6 and I 7 the red xy bands in the *middle* are pure, while the dark-red \tilde{xy} bands at the *bottom* are perturbed by the xz and yz valence and conduction bands. The $(\mathbf{k}, \mathbf{k} + \mathbf{c}^*)$ hybridization of the \tilde{xy} bands is seen to effectively extend over a k_c region of width 0.3 around the BZ boundaries, $k_c = 1/2 + \text{integer}$. The zero of energy is the center of the gap in the xz and yz bands, whereby $E_F = 75$ meV (see Sec. I VI). The occupation factor $\theta(\omega)$ in Eq. (10) removes the intensity from the bands with $E > E_F$.

As mentioned already in connection with Fig. I 10, the xy switching curves are even functions of κ_b whose sharpness decreases with increasing $|\kappa_b|$. That this holds also when dimerization distortion is included may be seen from Fig. 2 for $\kappa_a = 6.4$ by comparison of the switching curves for $\kappa_b = 0.225$, 0.250 and 0.275.

In Secs. III B and III C we shall explain how κ_a is deduced and how it is controlled by the photon energy, $h\nu$. From all Figs. 2–9, we thus conclude that, with proper m -dependent choice of the photon energy, the selection rule works well for

each of the three $\{\mathbf{k}, \mathbf{k} + \mathbf{c}^*\}$ pairs of quasi-1D t_{2g} bands in LiPB.

In paper III [2], we shall study the dispersion of the two quasi-1D bands in the gap and—as demonstrated by comparison of the red and dark-red bands in, respectively, the middle and bottom parts of Fig. 4—this requires that we take the weak hybridization of these xy -like bands with the xz and yz valence and conduction bands into account. This we do by downfolding those characters into the tails of the xy WOs, which thereby attain longer range and become what we call \tilde{xy} WOs. The concomitant modification of the WO form factor—and, hence, dimerization phase shift—we neglect. What the weak hybridization primarily changes is the *dispersion* of the \tilde{xy} energy bands. As mentioned before, a main goal of the present and the following paper III is to detect with ARPES the predicted dispersion in the perpendicular (k_c) direction, most noticeably the resonance peaks in the upper \tilde{xy} band caused by the weak hybridization with the yz and xz bands and expected to be seen near, respectively, $\kappa_c = -0.75$ and 0.75 . To see *both* the former resonance peak *and* its cause, the lower yz band, in the *same* ARPES experiment like in the theoretical Fig. 4 is, however, impossible because the former requires using $\kappa_a \approx 7.2$ and the latter $\kappa_a \approx 4.5$.

The Brillouin-zone-dependent photoemission intensity derived and discussed here based on a structure- and a form factor should be generally applicable to different materials. The main approximation made is in Eq. (1), where we approximate the wave-function of the photo-emitted electron by a plane wave. The free-electron state should in principle be a Bloch wave with an additional modification due to the sample surface. The approximation can become noticeable if the \mathbf{k} vector of the free electron is close to a zone boundary, where small periodic potentials are expected to gap degenerate free-electron states. A full understanding of the importance of describing the state of the photoelectron beyond a plane wave and including surface effects can be investigated with multiple-scattering techniques [8], but a simple intuitive picture is currently missing and should be further investigated. At the same time, calculations for graphene [3] or Bi_2Se_3 [9,10] assuming the photoelectron to be a plane wave seem to capture a large part of the Brillouin-zone-dependent intensity and agree well with experiment.

2. Wannier orbitals form factor $\tilde{w}_m(\boldsymbol{\kappa})$, inversion dimerization, and the coarse-grained structure

A t_{2g} WO $w_m(\mathbf{r})$ has a halo with contributions (tails) on the near Mo neighbors in the plane of this flat WO with the *same* m character as that of its head (see Figs. 5 and 9 in Paper I). For the present purpose, we neglect the hybridization between WOs with different values of m , as well as the details of the oxygens which $pd\pi$ antibond with the WO head and bond with the tail. What is important is that the head has a partial-wave shape, $Y_m(\hat{\mathbf{r}})\varphi_2(r)$, which is *translated* to the Mo n neighbors and multiplied by a factor, $c_n < 1$. This makes the FT $\tilde{w}_m(\boldsymbol{\kappa})$ of the WO *factorize approximately* into an orbital-dependent structure factor $\mathcal{S}_m(\boldsymbol{\kappa})$ times the FT of $Y_m(\hat{\mathbf{r}})\varphi_2(r)$:

$$\tilde{w}_m(\boldsymbol{\kappa}) \propto \mathcal{S}_m(\boldsymbol{\kappa}) \tilde{Y}_m(\hat{\boldsymbol{\kappa}}) \int_0^{0.55} j_2(2\pi\kappa r) \varphi_{\text{Mo}d}(r) r^2 dr. \quad (11)$$

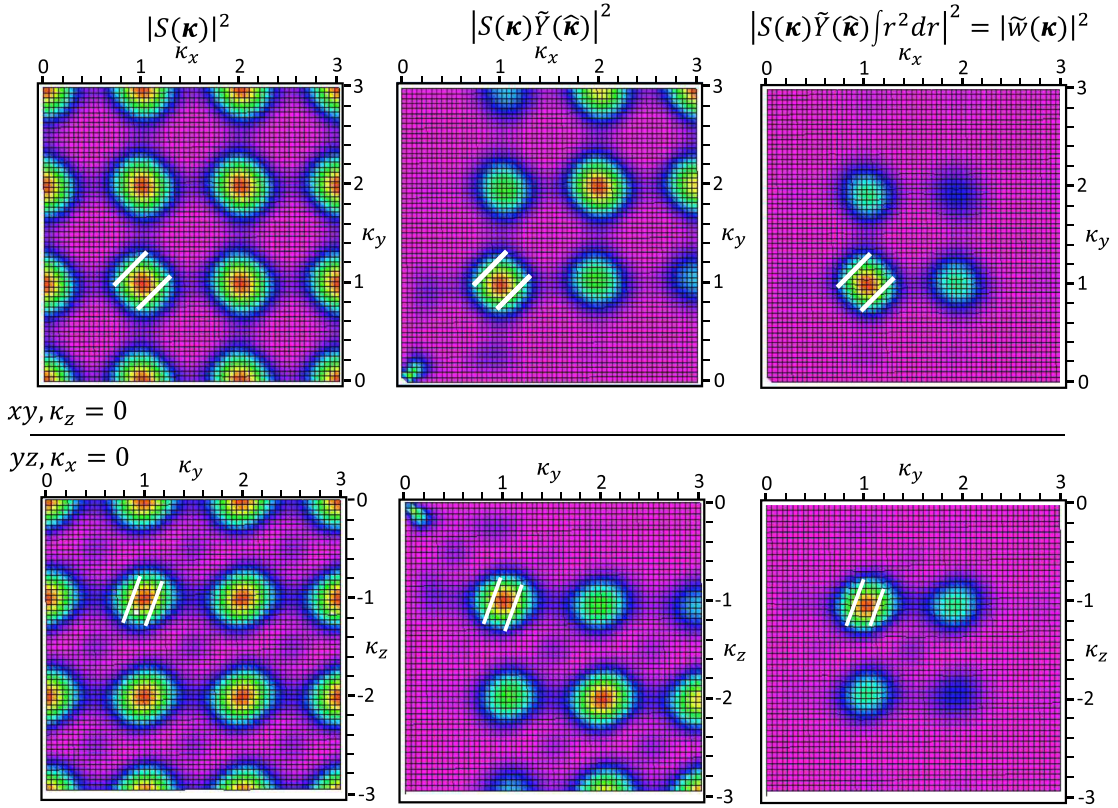


FIG. 5. Form-factor intensities $|\tilde{w}_m(\boldsymbol{\kappa})|^2$, i.e., the coarse-grained structure. *Top row*: xy form-factor intensities in the $\kappa_z = 0$ plane. (*bottom row*) yz form-factor intensities in the $\kappa_x = 0$ plane. $\tilde{w}_{xz}(\kappa_x, \kappa_y, \kappa_z) = \tilde{w}_{yz}(\kappa_y, \kappa_x, \kappa_z)$. (*columns 1–3*) Turning on factors following Eq. (11) with $S_m(\boldsymbol{\kappa})$ given by Eqs. (12) and (13). The little white lines are the projections onto the $\kappa_z = 0$ plane or the $\kappa_x = 0$ plane of the near-FS lines $|\kappa_b| \approx 1/4$, limited to the double zone $-1 \leq \kappa_c \leq 1$, along which the bands and fine-grained intensities for $\kappa_a = 6.4$ were plotted in Fig. 4. The κ_a, κ_b , and κ_c directions are those of, respectively, $\kappa_x + \kappa_y - \kappa_z, \kappa_y - \kappa_x$, and $\kappa_x + \kappa_y + 2\kappa_z$, see Eq. (15).

We have not computed the form factor by accurate, numerical FT of the WO,⁵ but shall use the factorization (11) together with the real-space figures to provide a qualitative *understanding* of the ARPES data to be presented in the following section.

Whereas the radial and angular factors $\int_0^{0.55} j_2(2\pi\kappa r)\varphi_{\text{Mol}}(r)r^2 dr$ and $\tilde{Y}_m(\hat{\mathbf{k}})$ are even, real functions of $\boldsymbol{\kappa}$, the structure factor $S_m(\boldsymbol{\kappa})$ is a complex function whose real and imaginary parts, like those of $\tilde{w}_m(\boldsymbol{\kappa})$, are respectively even and odd. From the WO figures I 5, with the xyz directions given by Charts I (14) and I (15), or Charts I (33) and I (34), we estimate these structure factors (the c_n coefficients) to be

$$S_{xy}(\boldsymbol{\kappa}) \sim \begin{bmatrix} +\frac{1}{2}e^{2\pi i\kappa_y} & +\frac{1}{6}e^{2\pi i(\kappa_x + \kappa_y)} \\ +\frac{1}{4}e^{-2\pi i\kappa_x} & 1 & +\frac{1}{2}e^{2\pi i\kappa_x} \\ +\frac{1}{4}e^{-2\pi i\kappa_y} & & \end{bmatrix} \bigg/ \left(1 + \frac{1}{2} + \frac{1}{2} + \frac{1}{4} + \frac{1}{4} + \frac{1}{6}\right), \quad (12)$$

⁵It may be kept in mind [see text after Eq. I (34)] that our t_{2g} WOs are given by the exact crystal structure and are insensitive to the orientation of the xyz system I (12), which is only approximately Cartesian.

$$S_{yz}(\boldsymbol{\kappa}) \sim \begin{bmatrix} +\frac{1}{8}e^{2\pi i(\kappa_z - \kappa_y)} & +1e^{2\pi i\kappa_z} & 0 \\ +\frac{1}{3}e^{-2\pi i\kappa_y} & 1 & +\frac{1}{2}e^{2\pi i\kappa_y} \\ 0 & +\frac{1}{4}e^{-2\pi i\kappa_z} & 0 \end{bmatrix} \bigg/ \left(1 + 1 + \frac{1}{2} + \frac{1}{3} + \frac{1}{4} + \frac{1}{8}\right), \quad (13)$$

and $S_{xz}[\kappa_x, \kappa_z] = S_{yz}[\kappa_y, \kappa_z]$.

In Fig. I 5 we clearly see that the inversion symmetry of the xy WO around its center Mo1 is far better preserved than that of the yz WO. The inversion dimerization is $w_m(-\mathbf{r}) - w_m(\mathbf{r})$, and the phase shift (9) due to inversion dimerization is $2 \arg \tilde{w}(\boldsymbol{\kappa}) = 2 \arg S(\boldsymbol{\kappa})$. The latter function is easily found from Eq. (12) for xy and from (13) for yz and was used to produce Figs. 2 and 3. Since $S_{xz}[\kappa_x, \kappa_z] = S_{yz}[\kappa_y, \kappa_z]$, we have $\eta_{xz}[\kappa_x, \kappa_z] = \eta_{yz}[\kappa_y, \kappa_z]$.

The structure factors S_{xy} , S_{yz} , and S_{xz} peak—with value one if the normalizations are as above—along the respective lines $[\kappa_x, \kappa_y, \kappa_z] = [L, M, \kappa_z]$, $=[\kappa_x, M, N]$, and $=[L, \kappa_y, N]$ passing through the respective points $L\mathbf{x}^* + M\mathbf{y}^* + N\mathbf{z}^*$ of the lattice reciprocal to the lattice I (12) with 1 Mo per primitive cell. In other words, $|S_{xy}|^2$, $|S_{yz}|^2$, and $|S_{xz}|^2$ form 2D square lattices of “beams” running in, respectively the κ_z, κ_x , and κ_y directions (see Fig. 5). This gives rise to intensity patterns that are *coarser* than the zone-selection patterns ($M + N$ even

or odd) whose origin is the smallness of the dimerization which increases the size of the primitive cell from 6 to 12 molybdenums.

The relation between the $[\kappa_x, \kappa_y, \kappa_z]$ and the $(\kappa_a, \kappa_b, \kappa_c)$ components—used to describe, respectively, the WO and the band structure and, hence, the coarse and the fine-grained structure—is

$$\kappa_x = \frac{\kappa_a + \kappa_c}{6} \mp \frac{\kappa_b}{2} \text{ and } -\kappa_z = \frac{\kappa_a + \kappa_c}{6} - \frac{\kappa_c}{2}, \quad (14)$$

which is the same as the transformation I (12) between the primitive translations of the approximately cubic Mo_1 and the exact Mo_{12} lattice [see also Charts I (14) and I (15)]. The inverse transformation—the same as I (13)—is

$$\begin{aligned} \kappa_a &= 2(\kappa_x + \kappa_y - \kappa_z), \\ \kappa_b &= \kappa_y - \kappa_x, \text{ and } \kappa_c = \kappa_x + \kappa_y + 2\kappa_z. \end{aligned} \quad (15)$$

Since exchange of κ_x and κ_y merely causes κ_b to change sign, $\mathcal{S}_{xz}(\kappa_a, \kappa_b, \kappa_c) = \mathcal{S}_{yz}(\kappa_a, -\kappa_b, \kappa_c)$.

The angular factors $\tilde{Y}_m(\boldsymbol{\kappa})$ in expression (11) have the same orientation with respect to the $a^*b^*c^*$ system as $Y_m(\hat{\mathbf{r}})$ has with respect to the abc system seen in Fig. I 5 and Charts I (14)–(15). This is so because the abc system is (almost) orthogonal (Sec. I III), whereby \mathbf{a} is parallel with \mathbf{a}^* , \mathbf{b} with \mathbf{b}^* , and \mathbf{c} with \mathbf{c}^* . As a result,

$$\tilde{Y}_{xy} \propto -\frac{\kappa_x \kappa_y}{\kappa^2} = \left(\frac{\kappa_b}{2\kappa}\right)^2 - \left(\frac{\kappa_c + \kappa_a}{6\kappa}\right)^2, \quad (16)$$

where

$$\kappa^2 \equiv \kappa_x^2 + \kappa_y^2 + \kappa_z^2 = \frac{1}{12}\kappa_a^2 + \frac{1}{2}\kappa_b^2 + \frac{1}{6}\kappa_c^2, \quad (17)$$

and similarly for \tilde{Y}_{yz} and \tilde{Y}_{xz} . The angular factor extinguishes the intensity around the $[0, 0, \kappa_z]$, $[\kappa_x, 0, 0]$, or $[0, \kappa_y, 0]$ lines, as is clearly seen when proceeding from the first to the second column in Fig. 5.

The last, radial factor in Eq. (11) is independent of m and merely gives the overall shape of the ARPES intensity. We found it sufficient to mimic the main part of the $\text{Mo } 4d$ radial function, continued for $r > 0.5$ (in units of 3.82 \AA) as the $t_{2g,m}$ average of the neighboring $pd\pi$ antibonds, by $\varphi_2(r) \propto (e^{-14r} - e^{-7})r^2$. This function peaks at $r \approx 0.14$, has at node at 0.5 , and is truncated at 0.55 . The negative part mimics the contribution from the $pd\pi$ antibonds. The last factor in (11) thus rises quadratically from $\kappa = 0$ and peaks at $\kappa \approx \sqrt{3}$, which is at the sphere passing through $[1, 1, -1]$. For larger values of κ , the radial factor decreases monotonically and for $\kappa \gtrsim 3$, i.e., outside the sphere passing through $[1, 2, -2]$ and $[2, 1, -2]$, it has fallen to below one third its value at the peak. The radial factor has been included in the two last columns of Fig. 5.

We thus realize that the angular and radial factors leave intensity in only small parts of reciprocal space.

The xy form-factor intensity $|\tilde{w}_{xy}(\boldsymbol{\kappa})|^2$ shown in the first row and third column in Fig. 5, has *one dominant peak*; its position is at $[\kappa_x, \kappa_y] = (1 + \frac{\epsilon}{6})[1, 1]$, where the small shift away from $[1, 1]$, proportional to $\epsilon \approx 0.4$, is mainly due to the angular factor. In three dimensions (3D), and according to Eq. (15), this peak becomes a beam centered on the line

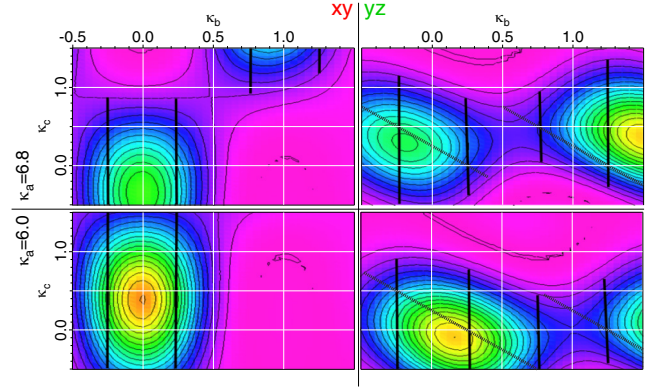


FIG. 6. Theoretical xy (left) and yz (right) coarse-grained ARPES intensity distributions $\kappa_a^2 |\tilde{w}_m(\boldsymbol{\kappa})|^2$ in the $\kappa_b\kappa_c$ planes with $\kappa_a = 6.0$ (bottom) and 6.8 (top) planes. The xz intensities equal the yz intensities mirrored around $\kappa_b = 0$. See the top part of Fig. 4 and Eqs. (10) and (18)–(22). The contours go from 0 to 400 in steps of 20. The black lines extending where the intensity exceeds 40 indicate xy and yz CECs with energy respectively 0.1 and 0.5 eV below the Fermi level (see Fig. 10) and in the periodic zone scheme.

given by

$$\kappa_a + \kappa_c = 6 + \epsilon \text{ and } \kappa_b = 0. \quad (18)$$

This holds as long as the κ_z dependence from the radial factor can be neglected. There are two less-intensive peaks near $[\kappa_x, \kappa_y] = [1, 2]$ and $[2, 1]$, which in 3D become beams around the lines given by

$$\kappa_a + \kappa_c = 9 \text{ and } \kappa_b = \pm 1. \quad (19)$$

In Fig. 6 we show the intensity distributions⁶ $\kappa_a^2 |\tilde{w}_m(\boldsymbol{\kappa})|^2$ in the planes with $\kappa_a = 6.0$ and 6.8 in the region $-0.5 \leq (\kappa_b, \kappa_c) \leq 1.5$. In the left-hand panel, we see the xy beam (18) form spots around the points $(\kappa_b, \kappa_c) = (0, \epsilon)$ and $(0, \epsilon - 0.8)$ when hitting the $\kappa_a = 6.0$ and 6.8 planes. In the latter plane, the less intensive spot centered near $(\kappa_b, \kappa_c) = (1, 2.2)$ and formed by the positive- κ_b beam (19) can be barely seen.

The yz form-factor intensity of zone selection, shown in the second row and third column in Fig. 5, has its *dominant peak* near $[\kappa_y, \kappa_z] = [1, -1]$. In 3D, this peak becomes a beam centered on the line given by

$$\kappa_a - 2\kappa_c = 6 \text{ and } \kappa_b + \kappa_c = 0. \quad (20)$$

There are two weaker peaks at $[\kappa_y, \kappa_z] = [2, -1]$ and $[1, -2]$, which in 3D become beams centered along the lines given by, respectively,

$$\kappa_a - 2\kappa_c = 6 \text{ and } \kappa_b + \kappa_c = 2, \quad (21)$$

and

$$\kappa_a - 2\kappa_c = 12 \text{ and } \kappa_b + \kappa_c = -2. \quad (22)$$

In the right-hand panel of Fig. 6 we see the yz beam (20) form spots around $(\kappa_b, \kappa_c) = (0, 0)$ and $(-0.4, 0.4)$ upon hitting the

⁶We take the polarization factor $\boldsymbol{\kappa} \cdot \hat{\mathbf{e}}$ as κ_a because this is about six times larger than κ_b and κ_c , and because the e_a component of the polarization (23) is much larger than e_b and e_c .

$\kappa_a = 6.0$ and 6.8 planes, as well as the beam (21) hitting these two planes at, respectively, $(\kappa_b, \kappa_c) = (2, 0)$ and $(1.6, 0.4)$.

The vertical and diagonal black lines, periodically repeated but limited to the regions where the intensity exceeds 40 in the units used in Fig. 4, indicate the constant energy contours (CECs) with binding energy 0.1 eV for xy and 0.5 eV for yz . The CECs will be discussed in the experimental section III D.

Since the xz form-factor intensity is related to the one shown for yz in Fig. 6 by a sign change of κ_b , we can see that, only for $\kappa_a \approx 6.4$ do the zx and yz intensities along, e.g., the P'QPQP' ($0.225, \kappa_c$) line, reach roughly the same maximum value. This is the maximum at ≈ 250 seen in the top part of Fig. 4 and in the third column of Fig. 3.

Our ARPES measurements, to be presented and discussed in the following section, were mainly performed in the neighborhood of the point $[\kappa_x, \kappa_y, \kappa_z] = [1, 1, -1]$ which is close to the peaks of all three form factors and which is the Γ point $(\kappa_a, \kappa_b, \kappa_c) = (6, 0, 0)$. It may be noted that, upon going from the first to the second column in the first row of Fig. 5, the angular factor sharpens up the $[1, 1]$ peak of the xy intensity. The traces of the two FS sheets, $|\kappa_b| = 1/4$, on the $\kappa_a = 6.4$ plane and bound between the $\kappa_c = \pm 1$ planes are the little white lines in Fig. 5, when projected onto the $\kappa_z = 0$ plane in the first row and onto the $\kappa_x = 0$ plane in second row. These are the P'QPQP' lines along which the intensity distributions were shown in Fig. 4. Since the xy band disperses in the direction of the κ_b lobe of its WO, this direction is perpendicular to the little white lines.

At the end of this long section II, we emphasize the following two points:

Whereas the k_a dependence of the $|\mathbf{k}$ -projected bands, i.e., of the fine-grained structure, is negligible compared with the k_b and k_c dependencies, the κ_a dependence of the aperiodic form factors, $|\tilde{w}_m(\boldsymbol{\kappa})|^2$, i.e., of the coarse-grained structure, is strong, as strong as the dependence on κ_c for xy , and half as strong for yz/xz , see Eqs. (18)–(20). This is due to the form factors being 2D $\propto \kappa_x \kappa_y, \kappa_y \kappa_z$, or $\kappa_x \kappa_z$, and to the orientation of the t_{2g} orbitals with respect to the crystallographic axes I (13).

Since the low-energy WOs in LiPB are relatively extended (covering several atoms), the radial part of the WO form factors make the beams narrow and thus cause the ARPES intensity to depend rather strongly on the photon energy $h\nu$, as we shall see in Sec. III C.

III. PRESENTATION AND DISCUSSION OF THE ARPES DATA

From the basics of the electronic structure in Sec. I IV we expect the two $\tilde{x}\tilde{y}$ bands crossing the Fermi level to have by far the largest dispersion with k_b , i.e., along the ribbon, weak dispersion with k_c , i.e., up and down the staircase, weak k_c -dependent splitting caused by direct inter-ribbon hopping and by hybridization with the gapped xz and yz bands, and essentially no dispersion with k_a due to the lack of hopping between staircases. In the following, we want to demonstrate that this strong one dimensionality is indeed confirmed by our ARPES experiment. We also pay attention to the aperiodic variations of the ARPES intensity between equivalent zones and compare them with the coarse-grained intensity variations predicted in the preceding Sec. II B 2. The fine-grained inten-

sity variations (zone selection) predicted in Sec. II B 1 will be observed in Secs. III D and III E where, most importantly, we also compare the band dispersions in detail with those predicted by the LDA as parametrized by the t_{2g} TB Hamiltonian (Sec. I VI).

Intensity variations and one dimensionality are also features of the ARPES yz and xz bands, but of course not near the Fermi level where they are gapped. Moreover, their one dimensionality is with $k_c + k_b$ or $k_c - k_b$ rather than with k_b .

A. ARPES method

We measured several samples for the conclusions presented in this work. The samples came from two different crystal growers and were all prepared by a temperature gradient flux growth technique [11]. In the text, we refer to two samples G (Greenblatt) and H (He) representing the variation detectable in our experiments.

Photoemission measurements were performed at the MER-LIN endstation (BL 4.0.3) of the Advanced Light Source with a Scienta R4000 electron detector. The polarization was set to linear vertical, i.e., in Fig. 10 the vector of the electric field is horizontal. The temperature was set to $T = 26$ K for sample G and $T = 6$ K for sample H and the samples were cleaved while attached to the cold manipulator at $p \approx 4 \times 10^{-11}$ torr. The overall energy resolution was set to around 16 meV at photon energy $h\nu = 30$ eV going up to around 40 meV at $h\nu = 100$ eV. At $h\nu = 30$ eV, the momentum resolution in the \mathbf{b}^* direction is 2% of k_{Fb} at half filling (i.e., at nominal Li₁ stoichiometry), i.e., 0.005. With the solid-state definition of reciprocal space [see Paper I, Sec. III below Eq. (11)], this is 0.006 \AA^{-1} . The polarization vector in sample coordinates is

$$\frac{\mathbf{E}}{|\mathbf{E}|} = \begin{pmatrix} e_a \\ e_b \\ e_c \end{pmatrix} = \begin{pmatrix} \sin(65^\circ - \phi) \cos \theta \\ \sin(65^\circ - \phi) \sin \theta \\ \cos(65^\circ - \phi) \end{pmatrix}. \quad (23)$$

Here, ϕ is the polar rotation, and the θ is the tilt angle. In our measurements, $|\phi| \lesssim 5^\circ$ and $|\theta| \lesssim 5^\circ$, resulting overall in a strong component along the \mathbf{a} axis, normal to the cleavage plane, a weak component along the \mathbf{c} axis, and a very weak component along the \mathbf{b} axis.

LiMo₆O₁₇ is susceptible to oxygen loss caused by intense ultraviolet light where the desorption is due to the Knotek-Feibelman mechanism including a core-level excited resonant Auger decay [12]. It shares this behavior with, e.g., NaMo₆O₁₇ [13], K_{0.3}MoO₃ [14], or oxides like TiO₂ [15] and SrTiO₃ [16,17]. We were not able to prevent this damage by oxygen dosing (which is possible, for example, for SrTiO₃ [17]). The reason might be the existence of both tetrahedral- and octahedral-coordinated molybdenums. A small oxygen loss causes a slight electron doping but, as time progresses, the ARPES signal eventually blurs. To prevent the loss, one concept might be to keep the photon energy below that of the lowest-energy core level resonance. However, often there is higher-order light that still causes a slow degradation (with the timescale in the hours instead of minutes) and therefore our concept is to use a large homogenous area and slightly alter the position of the beam spot when the sample degradation begins.

Even though the ARPES lineshapes have the general 1D holon-peak and spinon-edge features [18], they were analyzed by a model-free method described in detail in paper III Sec. II B [2]. This procedure was necessitated because the low- T ARPES lineshape is not sharp enough to agree in detail with the low- T transform-limited lineshape [19]. If the transform-limited lineshape is broadened ad hoc it can be made to fit [18], but we did not want to use that ad hoc procedure in the current work.

B. Ansatz for deducing κ_a

We repeat here some basics of ARPES, cf. Refs. [20,21] As in Sec. II A we use a notation according to which \mathbf{k} denotes the Bloch vector in a (periodically repeated) single zone of an initial state, and κ is the momentum of the final plane-wave state *inside* the crystal. According to Eq. (10), $\kappa \text{ [mod zone]} = \mathbf{k}$. Upon leaving the crystal, the photoelectron is diffracted in the direction away from the surface, whereby the normal momentum component $\kappa_{\perp} = \kappa_a \mathbf{a}^*$ jumps discontinuously to a smaller value $\kappa_{\perp o}$. Parallel to the surface, the momentum is conserved:

$$\kappa_{\parallel} \equiv \kappa_b \mathbf{b}^* + \kappa_c \mathbf{c}^* = \kappa_{\parallel o}.$$

What is measured in ARPES is, for a given photon energy $h\nu$, the yield I , the angle of exit θ , and the kinetic energy $T = \frac{\hbar^2}{2m} |\kappa_o|^2$ of the photoelectrons in the analyzer *outside* the crystal. The value of κ_a inside the sample is deduced from the two latter quantities by assuming that, inside the crystal, the energy of the final state is $V + \frac{\hbar^2}{2m} |\kappa|^2$, i.e., the energy of an electron, free with respect to a potential floor V , and that outside the crystal, the momentum is

$$\kappa_o = (\kappa_{\perp o}, \kappa_{\parallel}) = \frac{\sqrt{2mT}}{h} (\cos \theta, \sin \theta), \quad (24)$$

and the energy is $\Phi + T$. Here, Φ is the work function of the sample. It should not be confused with $\Delta\Phi$ which is a constant given by the apparatus and is essentially the difference between the work function of the sample and analyzer. $\Delta\Phi$ allows us to relate the measured kinetic energy to the binding energy ω within the sample,

$$\omega \equiv -E_j(\mathbf{k}) = h\nu - (\Delta\Phi + T). \quad (25)$$

Equating the inside and outside energies yields the desired relation for κ_a :

$$\frac{\kappa_a}{a} = |\kappa_{\perp}| = \frac{\sqrt{2m}}{h} \sqrt{T \cos^2 \theta + V_0}, \quad (26)$$

where $V_0 \equiv \Phi - V$ is the so-called *inner potential*. Taking V and Φ with respect to the Fermi level, which is common for the crystal and the analyzer, V is negative and Φ is positive, whereby V_0 is positive. Its value is determined empirically.

C. Photon energy dependence

1. Fermi surface intersection with $\mathbf{a}^*\mathbf{b}^*$ planes

We begin by showing ARPES for photoelectrons coming from slightly below the Fermi level, i.e., from the $\tilde{\chi}$ electrons. Figure 7 shows for sample H at $T = 6$ K the photoelectron yield as a gray-scale intensity, a so-called FS map, in the three

$\kappa_a \kappa_b$ planes with $\kappa_c = 0, 1/4$, and $1/2$, colored respectively blue, red, and green. In the $\kappa_c = 0$ plane, the scan covers many BZs. We see the traces of the two FS sheets separating the occupied states, $|k_b| < k_F$, between the sheets from the empty states, $|k_b| > k_F$, outside the sheets. These traces appear as straight lines and are thus consistent with being the intersections with a $\kappa_a \kappa_b$ plane of a 1D nearly-half-filled FS, $|k_b| = k_F \approx 1/4$. This FS is seen to be periodic in the $\mathbf{a}^*\mathbf{b}^*\mathbf{c}^*$ lattice and to have aperiodic, coarse-grained intensity variations.

Since the κ_a direction is perpendicular to the plane of the sample, it must be accessed by variation of the photon energy. For presenting these measurements, we converted our raw yield I and kinetic-energy T data as functions of angle θ and photon energy $h\nu$, as explained above, to binding energy ω and momentum vector κ using the value $V_0 = 11$ eV for the inner potential. With the work function of the sample being $\Phi = 4$ eV, the potential floor is thus 7 eV below the Fermi level, i.e., $V = -7$ eV. The dotted constant- $h\nu$ circles in Fig. 7 are the cross sections of the sphere $V + \frac{\hbar^2}{2m} |\kappa|^2 = h\nu$ with the constant- κ_c planes. For a given $h\nu$, normal emission ($\theta = 0 = \kappa_b = \kappa_c$) from the Fermi level⁷ thus has the κ_a value

$$\kappa_a(0, 0, h\nu) = \frac{a\sqrt{2m}}{h} \sqrt{h\nu - V} \approx 7.0 \sqrt{\frac{h\nu + 7 \text{ eV}}{40 + 7 \text{ eV}}}, \quad (27)$$

which, as expressed on the right-hand side, is 7.0 for $h\nu = 40$ eV.

Figure 7(a) shows intensity variations in central ($\kappa_c = 0$) plane: Strong intensity in the region $(\kappa_a, \kappa_b) = (5.5-7.5, \pm k_F)$ and weak intensity in the regions $(8.0-10.5, \pm(1 \pm k_F))$. In the former, we see an intensity variation with minimum at the zone boundary ($\kappa_a = 6.5$). In the last-mentioned regions, the intensity along the FS is weak and fairly constant. In Fig. 7(b), the $\kappa_c = 1/4$ plane, which contains the resonance peak (see bottom part of Fig. 4), the intensity variation seems to be shifted a bit, and again in Fig. 7(c) to be in register with the variation in Fig. 7(a).

The qualitative theory of the coarse-grained intensity variations presented in Sec. II B 2 associate them with the form factor of the xy WO in the present case. The theory yields the result shown in Fig. 8 which compares quite well with the experimental Fig. 7(a). We thus realize that the region of strong intensity is due to the beam (18) whose center hits the $\kappa_c = 0$ plane at $(\kappa_a, \kappa_b) = (6.4, 0)$, and that the two regions of weak intensity are due to the beams (19) causing the spots at $(\kappa_a, \kappa_b) = (9, \pm 1)$.

Apart from the observed coarse-grained intensity variations, we confirm that, slightly below the Fermi level there is no dispersion along κ_a , i.e., there is strongly reduced dimensionality in the \mathbf{a}^* direction.¹¹⁵ The intensity variation seen as a function of κ_a in Fig. 7 has period one in κ_a and is, therefore, *not* the fine-grained intensity variation (zone selection) described in Sec. II B 1, which has period two in κ_c and is due to emission from *one* of the two xy bands. The

⁷For finite binding energy, $h\nu$ should be substituted by $h\nu - \omega$ in Eq. (27). But even going to the bottom of the band, where $\omega = 0.7$ eV, this lowers κ_a by merely ≈ 0.06 .

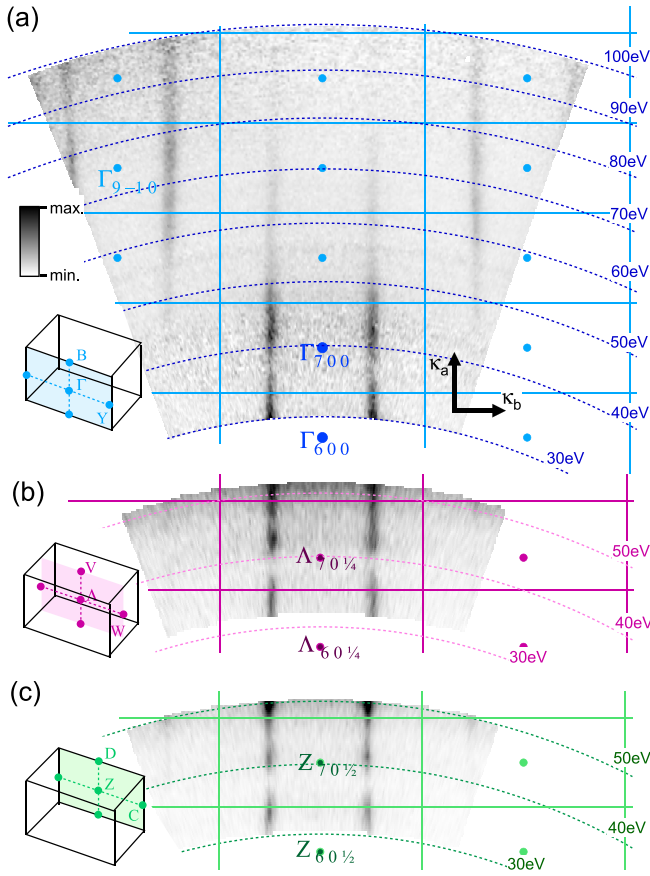


FIG. 7. Photon energy scan of sample H at $T = 6$ K for κ_c in three $\mathbf{a}^*\mathbf{b}^*$ planes: (a) FS map through $\kappa_c = 0$ (Γ BY) (b) $\kappa_c = 1/4$ (Λ WV), and (c) $\kappa_c = 1/2$ (ZDC). The full colored lines along \mathbf{a}^* and \mathbf{b}^* are the intersections with the BZs. The blue dotted lines intersect at the reciprocal-lattice points Γ_{LMN} . The high-intensity traces represent the 1D FS showing no dispersion in the \mathbf{a}^* direction. There are coarse-grained intensity variations whose origin is the structure factor of the form factor for the xy WOs, see Sec. II B 2 and Fig. 8. This figure and the following are approximately to scale, i.e., consistent with $a/b = 2.31$.

intensity seen could, in principle, be due to k_a dispersion,¹¹⁵ but this, we judge, is far too weak, so we currently have no explanation.

In the \mathbf{c}^* direction, i.e., from Figs. 7(a)–7(c), the dispersion is very weak. That there are two bands at the Fermi level and the FS therefore has two close-lying Fermi vectors, $k_{Fu} = k_{F2}$ and $k_{Fl} = k_{F1}$ along κ_b , cannot be seen in these figures, but might, in principle, be resolved because the resolution is 16 meV when $h\nu = 30$ eV (and decreases to 40 meV when $h\nu = 100$ eV).

2. Fermi surface intersection with $\mathbf{b}^*\mathbf{c}^*$ planes; $h\nu = 30, 33,$ and 37 eV

Like in Fig. 7, the intensity for photoelectrons coming from slightly below the Fermi level is shown in Fig. 9, but now in the $\kappa_b\kappa_c$ plane, over two BZs ($|\kappa_b| \leq 1/2$, $|\kappa_c| \lesssim 1$), and for $h\nu = 30, 33,$ and 37 eV. The coarse-grained intensity is seen to change significantly over this range of photon energies, and only for 33 eV does it extend over both

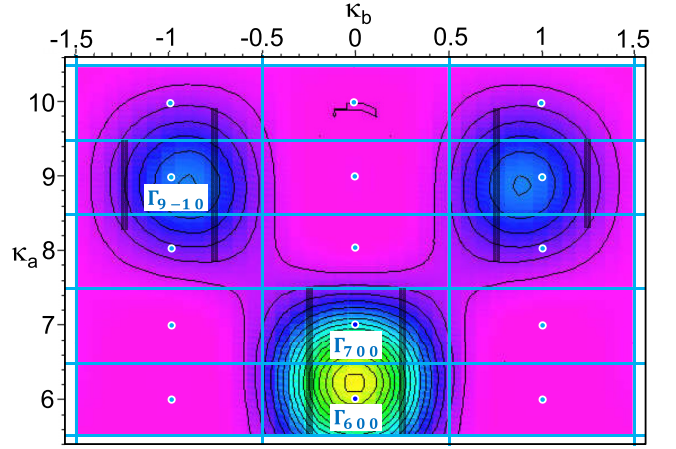


FIG. 8. Theoretical ARPES intensity distribution $\kappa_a^2 |\tilde{w}_{xy}(\kappa_a, \kappa_b, \kappa_c = 0)|^2$ to be compared with the coarse-grained part of the experimental intensity distribution in Fig. 7. The contours go from 0 to 400 in steps of 20. The black lines indicate the traces of the near-FS sheets, $|\kappa_b| \approx 1/4$, in the periodic zone scheme and extend where the intensity exceeds 40.

BZs. This we can partly understand from the $h\nu$ dependence of κ_a .

For the three photon energies, Eq. (27) yields, respectively, $\kappa_a(0, 0, h\nu) = 5.9, 6.2,$ and 6.5 , which according to the simplest prediction (18) of the κ_c position of the intensity maximum (seen on the left-hand side of Fig. 6 for $\kappa_a = 6.0$ and 6.8) for the xy beam gives: $\kappa_c = 0.5, 0.2,$ and -0.1 , as compared with $0.2, \approx 0,$ and -0.6 estimated from the experimental Fig. 9. The latter κ_c values correspond via Eq. (18)

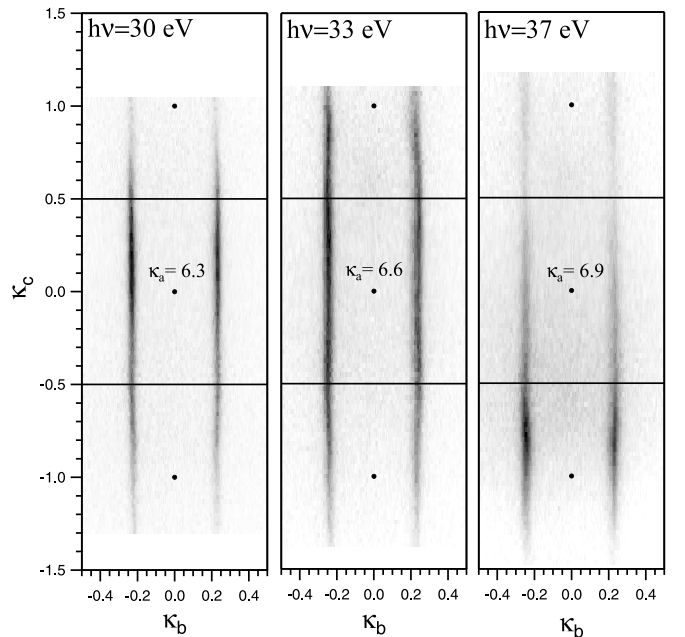


FIG. 9. FS map at different photon energies $h\nu = 30, 33, 37$ eV. For $\kappa_b = \kappa_c = 0$, this is at $\kappa_a = 6.3, 6.6,$ and 6.9 , as indicated. These figures have been stretched along κ_c by a factor 1.7 [compare with Figs. 1 and 10(b), which are to scale].

to the somewhat larger κ_a values: 6.2, 6.4, and 7.0, whose intensity distributions can easily be imagined from those for $\kappa_a = 0$ and 6.8 shown on the left-hand side of Fig. 6. These do exhibit the remarkable contraction along κ_c of the experimental intensity distribution seen in Fig. 9 for the highest energy. On top of this comes the narrowing of the beam due the delocalization of the $\tilde{x}\tilde{y}$ WO caused by the down-folding of the valence- and conduction-band orbitals [see Eq. III (4)].

D. Constant-energy contours in the $\mathbf{b}^*\mathbf{c}^*$ plane

In Fig. 10 we present ARPES results for binding energies, ω , which takes us from the Fermi level to the bottom of the Mo 4d bands so that we also get to see the xz and yz valence bands. The results are shown in the 2D region ($0 \leq \kappa_b \leq 1/2$, $0 \leq \kappa_c \lesssim 1$) which with reference to Figs. 1 and 10(a) includes the upper half of the BZ centered at $\Gamma_{00} \equiv \Gamma$ plus the lower half of the one centered at $\Gamma_{01} \equiv \Gamma'$. We refer to these BZs as, respectively, the first and the second. Together, they form the upper part of the double zone centered at Γ . Here, “upper” and “lower” refer to the orientation which has κ_c pointing upward.

The rightmost panel in Fig. 10(b) shows ARPES as measured and the leftmost panel shows ARPES with the fine-grained (plus some of the coarse-grained) intensity variations symmetrized away by adding the intensities from both sides of the BZ boundary (CZC, $\kappa_c = \frac{1}{2}$), exploiting the equivalence⁸ of xz and yz . This corresponds to adding the intensities at \mathbf{k} and $\mathbf{k} + \mathbf{c}^*$.

The middle panel of Fig. 10 shows the CECs from the LDA-TB bands with the common energy of the four xz and yz WOs shifted downwards by 100 meV with respect to the energy of the two xy WOs [see Figs. 12(a) and 12(b)] in order to improve the agreement with the symmetrized ARPES in the rightmost panel. This agreement—down to every detail—is astonishing, and so is the straightness of the three sets of lines, even close to where they cross. The theoretical CECs have been colored red, blue, and green according to their respective xy , xz , or yz character, and in order to mimic the spectral-function broadening of the dispersion, the shifted LDA-TB bands were broadened by a Lorentzian with energy-independent width.

The CECs from the *symmetrized* ARPES and the shifted LDA-TB bands behave as described in paper I [1], Sec. IV A together with Figs. I 4, 6, 7, and 8. The upper part of the double zone is shown also in Fig. 1 of the present paper.

In Fig. 10 we recognize the CECs of the quasi-1D degenerate $xy(\mathbf{k})$ and $xy(\mathbf{k} + \mathbf{c}^*)$ bands (red) dispersing in the k_b direction with the distance $2k_b(E)$ between the two sheets increasing like $\approx(2/\pi)\sqrt{(E-B)/|t|}$ with $t \approx -1$ eV [see

⁸Note that, whereas the band structure is invariant to the individual mirror operations $k_b \rightarrow -k_b$ and $k_c \rightarrow -k_c$, the eigenfunctions are merely invariant to the inversion $(k_b, k_c) \rightarrow -(k_b, k_c)$. As a consequence, the above-mentioned even/odd symmetries around $k_c = -1, 0, 1$ and $k_c = 1/2$ do not hold for the blue and green curves individually, but only for their sums.

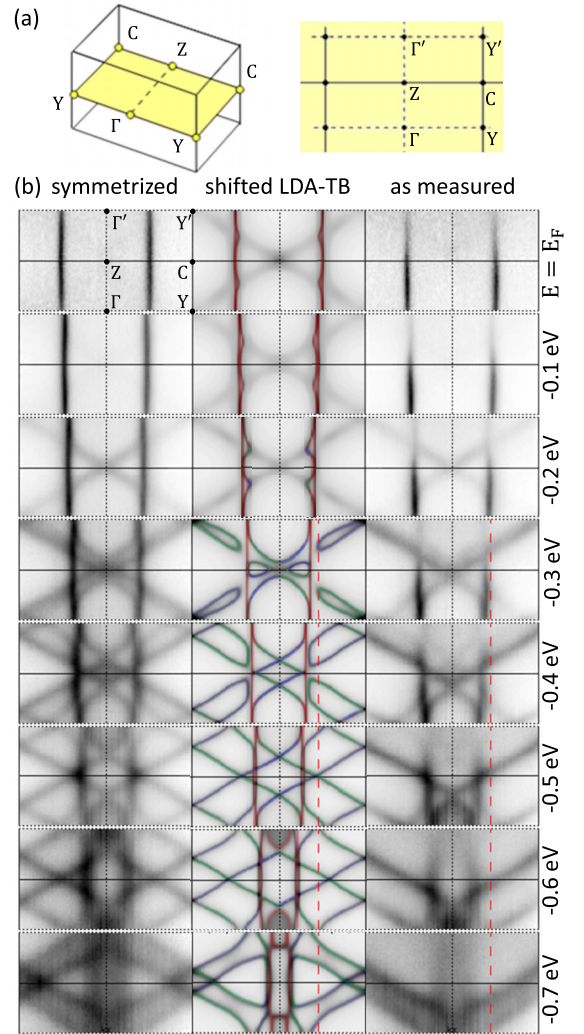


FIG. 10. (a) Orientation in the zone of the $\kappa_b\kappa_c$ plane with $\kappa_a = 6$. The CECs are shown in the upper part of the first BZ and the lower part of the second BZ: $|\kappa_b| \leq 1/2$, $0 \leq \kappa_c < 1$. See also Fig. 1. (b) Comparison of the CECs computed using the LDA-TB parameters, listed in Eqs. I (43)–(47) including the 100 meV shift, with those measured by ARPES for sample H ($T = 6$ K, $h\nu = 30$ eV). Red, blue, and green indicate dominating xy , xz , and yz character. The red dashed line ($k_b = 0.225$) is the one along which we often show bands, such as the $|\mathbf{k}$)-projected ones in Fig. 4. The match with the symmetrized ARPES is nearly perfect, and so is the prediction that in ARPES as measured, the xz and yz CECs are extinguished in the respective second zone, i.e., above the respective ZY' line. Indicated on the right are the energies with respect to the Fermi level.

Sec. I IV, Eq. I (23)] and heading towards $\approx 1/2$ at the Fermi energy.

The quasi-1D $xz(\mathbf{k})$ (blue) and $yz(\mathbf{k})$ (green) bands dispersing with, respectively, $k_c - k_b$ and $k_c + k_b$ [see Eq. I (27)], are degenerate at their common bottom at Γ where they are also nearly degenerate and hybridize with the two xy bands, thus giving rise to CECs which are complicated near Γ . For energies a bit above the common bottom of all three t_{2g} bands, $B \approx E_F - 0.75$ eV, the blue and green pair of CECs are parallel with and lie on either side of, respectively, the $k_c - k_b = 0$ and $k_c + k_b = 0$ lines. As the energy increases, so

does the distance $\approx (2/\pi)\sqrt{(E-B)/|A_1|}$ between each pair of parallel blue or green CECs. This distance is approximately $\sqrt{t/A_1} \approx 1.8$ times the one between the red xy CECs.

The blue and the green $\mathbf{k} + \mathbf{c}^*$ bands are shifted by $\Delta k_c = 1$ and thus behave in the same way as the respective blue and green \mathbf{k} bands. For energies above ≈ -0.5 eV, the closest CEC pairs are those on either side of the respective zone boundary, $|k_c + k_b| = 1/2$ or $|k_c - k_b| = 1/2$, onto which they coalesce when $E \sim E_F - 2|G_1| = E_F - 0.2$ eV. Here, $2G_1$ is the electronic dimerization causing a gap of $\pm 2G_1$ [see Eq. I (29) and Fig. I 6 for $k_b = 0.225$].

We are particularly interested in the hybridization of the xy bands inside the gap around E_F . It can be seen in theory by comparison of the light and the dark red bands in Figs. I 6 and I 7, respectively, or in the middle and bottom parts of Fig. 4 of the present paper II, and we study it in detail in paper III [2]. Although bands—and not CECs—hybridize, we can see the effect of this hybridization in the LDA-TB part of Fig. 10 at 0.1 and 0.2 eV below E_F as four “notches” pointing inward, toward Z, and we can follow them as the energy is lowered into the valence bands. The origin of the notches is clearly the energy repulsion between the hybridizing valence-band edge and one of the two degenerate xy bands; the other band is unaffected. Since the notch is sharp, it can only come from an edge of a nearby yz or xz band (but not from a far-away yz or xz band) with a weak matrix element, and as long as the notch points toward Z rather than Y, it comes mainly from the edge of the valence (V) rather than from the edge of the conduction (C) band. The corresponding peak is in the upper \tilde{xy} band (Fig. I 7) and we call it a *resonance peak*. (If we take the nearly dispersionless k_a dimension into account, the peak is a “mountain ridge” extending along \mathbf{a}^*).

According to the *selection rules* derived in Sec. II B 1 and illustrated in Fig. 4, ARPES *as measured* in Fig. 10(b) should see the occupied $|\mathbf{k}\rangle$ -projected bands in the first physical zone and the occupied $|\mathbf{k} + \mathbf{c}^*\rangle$ -projected bands in the second physical zone. With the blue xz and green yz bands gapped around the Fermi level, these bands should be seen in the first physical zone only, and comparison with Fig. 1 shows this to be the case. Specifically, the blue and green bands with $E < E_F - 0.2$ eV are extinguished in their respective second zone. The dimerization distortion of the yz (and xz) intensities for negative κ_c predicted in Fig. 3 for $\kappa_a = 6.4$, specifically the intensity enhancement near $\kappa_c = -0.4$ for the upper band was seen in the data; but this is outside the range of positive κ_c shown in Fig. 10(b).

For the red metallic xy bands, the Fermi sea inside the outer sheet should be seen in the first BZ and the sea inside the inner sheet should be seen in the second BZ, with a switch near the BZ boundary, $k_c = 1/2$. This means that the notches should be seen only in the second BZ, but the drop of intensity for $\kappa_c > 0.5$ in ARPES as measured with $h\nu = 30$ eV (Fig. 9) makes this observation difficult. We shall return to it in Sec. III B in paper III.

Herewith, we have arrived at the influence of the yz and xz form factors. In Fig. 10(b) we see that the intensity as measured for given binding energy (deep inside the valence bands) is slightly stronger for (green) $yz(\mathbf{k})$ than for $xz(\mathbf{k})$ (blue) and increases with κ_c in the range (0|1). As may be seen

from the theoretical Fig. 6, the former property is consistent with the behavior of $\kappa_a^2 |w_{yz}(\kappa)|^2$ for $\kappa_a \approx 6.4$, but the latter requires $\kappa_a \approx 7$.

E. Energy bands $E_j(k_b, k_c)$

In the preceding section, the CECs *as measured* were shown in the right-hand panel of Fig. 10(b) and were explained as the fine-grained, double-periodic $|\mathbf{k}\rangle$ projection of the occupied part of the lower m band in the first and of the upper m band in the second physical zone (see Sec. II B 1), on the background of the coarse-grained, aperiodic polarization and WO form-factor intensity $\kappa_a^2 |\tilde{w}_m(\kappa)|^2$ (see Sec. II B 2). Hence, the xz and yz bands were seen only in the respective first physical zone because their upper bands are empty and so were the metallic xy bands due to the drop of their polarization and form-factor intensity for $h\nu = 30$ eV ($\kappa_a = 6.3$) in the second BZ.

Figure 11(b) now displays the ARPES band structure as measured on the faces of a box with the basal (k_b, k_c) plane extending over the upper half of the double zone, like in Figs. 1 and 10. On the top face, i.e., for $E \sim E_F$, we recognize the 1D xy FS, $(k_b, k_c) \sim (\pm 1/4, k_c)$, with its intensity drop in the second BZ. Not only the xy bands are quasi 1D, but so are the xz and the yz bands: Had the box been cut at the top of the valence bands, we would—like in the rightmost panel of Fig. 10(b)—have seen their ridges follow the boundaries of their physical zones (Fig. 1).

The band structures shown in Figs. 11(d) and 11(e) are obtained by cutting the data along the lines colored in Fig. 11(a). To avoid the fine-grained intensity variations, we show in Fig. 11(c)—like in the leftmost panel of Fig. 10(b)—the band structure symmetrized over the first and second zones; the benefit of this symmetrization is evident! Had there been no coarse-grained intensity variations, this band structure would have been periodic in the BZ and have the rectangle ΓZCY ($0 \leq k_b \leq 1/2$, $0 \leq k_c \leq 1/2$) as its irreducible part. The symmetrized bands in Fig. 11(c) will be compared with the LDA band structure (Fig. 12) in the following Sec. IV and, subsequently, its TB parameters will be fine-tuned to achieve almost perfect agreement with the occupied ARPES bands.

The fine-grained intensity variations, on the other hand, hold the key to resolving the thus-far elusive splitting and warping of the nearly degenerate quasi-1D xy -like FS. But let us first test our understanding of the intensity variations by using it to explain the band structure *as measured* along the lines colored in Fig. 11(a) and shown in Figs. 11(b), 11(d), and 11(e).

Along $\Gamma Z\Gamma'(k_b = 0)$ we see the rise of the degenerate $xz(\mathbf{k})$ and $yz(\mathbf{k})$ valence bands from their bottom at $E_F - 0.75$ eV at Γ to their highest point, $E_F - 0.25$ eV, where the blue and green valence-band ridges cross at Z. Here, half their $|\mathbf{k}\rangle$ characters—and hence ARPES intensities—have been lost. On the downturn in the second zones, to Γ' , the $|\mathbf{k} + \mathbf{c}^*\rangle$ characters take over and the intensities drop accordingly. At $E_F - 0.75$ eV we also see the dispersionless bottom of the two degenerate xy bands and expect the intensity to shift from the lower to the upper band as we pass from the first to the second BZ. That the measured total xy intensity nevertheless

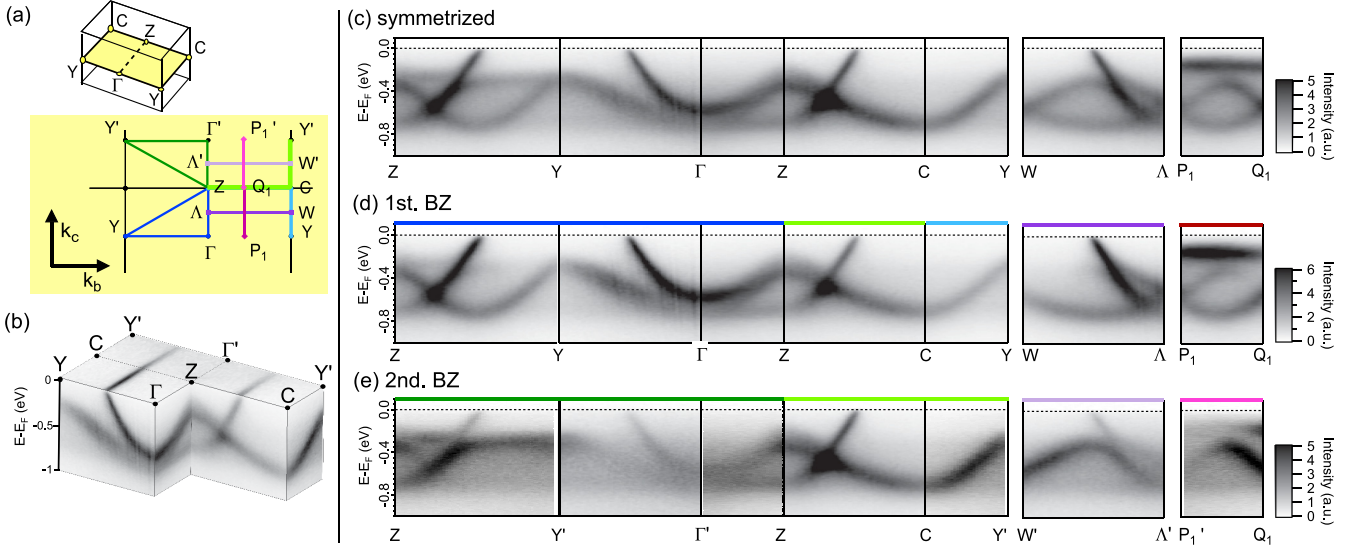


FIG. 11. ARPES band structure. (a) Orientation of half the first BZ in $\kappa_a\kappa_b\kappa_c$ space and, in the $\kappa_b\kappa_c$ plane, half the first BZ ($0 \leq \kappa_c \leq 1/2$) centered at Γ , and half the second BZ ($1/2 \leq \kappa_c \leq 1$) centered at Γ' . The BZ is the physical zone for the xy bands, and the physical zones for all three t_{2g} bands were shown in Fig. 1. (b) Data *as measured* from sample H ($T = 6$ K, $h\nu = 30$ eV) presented in an $E(\kappa_b, \kappa_c)$ box where cuts along the κ paths colored in panel (a) produce the band structures shown in panels (c)–(e). (d) Some features can be better seen in the first BZ, (e) while others are more pronounced in the second BZ, and vice versa. This is so because band selection follows the physical rather than the Brillouin zone (see Sec. VID in paper I [1]). (c) The symmetrized band structure shows all spectral features.

drops, we ascribe to the above-mentioned drop of the form factor in the second BZ.

When going inside the first zone from Γ to Y , the other crossing point of the blue xz and green yz valence band ridges (see Fig. 1), the $xz(\mathbf{k})$ and $yz(\mathbf{k})$ valence bands are seen to rise and lose intensity in a similar same way as they did toward Z , except that there—due to spin-orbit splitting (see Fig. 13)—the maximum was higher. The ΓY cut in the band structure is also shown on the front face of the box in Fig. 11(b). Intensity is prominently seen from the (lower) xy band rising parabolically from its bottom along ΓZ to the FS along $k_b \approx 1/4$. The aforementioned drop of xy intensity in the second BZ is clearly seen on the top face of the box. If we go inside the second zones from Γ' to Y' at the zone boundary, this is the only place where intensity from the valence bands is seen.

Along the green diagonal from Y' to Z , where the gapped $yz(\mathbf{k})$ and $yz(\mathbf{k} + \mathbf{c}^*)$ bands form the valence-band ridge, this ridge is clearly seen; in fact far better than the blue ridge from Y to Z formed by the gapped $xz(\mathbf{k})$ and $xz(\mathbf{k} + \mathbf{c}^*)$ bands. A similar intensity difference between yz and xz was also observed in Fig. 10 and was explained at the end of Sec. III D as due to different form factors. The xz band gives no intensity along the green $Y'Z$ line because it is in the second yz zone, which is empty. Returning now to the blue valence-band ridge along YZ , we see the yz band fall, reach its bottom halfway toward Z , and then rise again to the highest point on the ridge at Z . Here, the yz band not only attains $|\mathbf{k} + \mathbf{c}^*)$ character, but also hybridizes with the xz band via spin-orbit coupling. We also see the parabolic rise of the lower xy band from its bottom at Z toward Y , reaching E_F at half the way. Toward Y' , the xy intensity is reduced by the form factor.

Going along the BZ boundary from Z to C for k_b positive, the nearly degenerate xy bands rise and cross the Fermi level near $(1/4, 1/2)$ and the xz valence band falls from the highest point on the ridge to its bottom at C . At Z , the green yz band is degenerate with the blue xz valence band and has intensity there, which, however, vanishes after leaving the first green zone.

Upon going from C to Y' ($k_b = 1/2$) inside the blue xz zone, we see the xz band increase to the blue ridge at Y' . Going instead to Y , we see the other branch of the xz band increase to the blue ridge at Y .

Along ΛW ($k_c = 1/4$), the lowest band—with minimum at $(1/4, 1/4)$ —is the blue $xz(\mathbf{k})$ band. The $yz(\mathbf{k})$ band is degenerate with $xz(\mathbf{k})$ at Λ but then increases until at $(1/4, 1/4)$ it reaches the top of the green ZY ridge where it mixes with the $yz(\mathbf{k} + \mathbf{c}^*)$ band coming from W and thereby loses its intensity. Going instead from Λ' toward W' ($k_c = 3/4$), it is the blue $xz(\mathbf{k} + \mathbf{c}^*)$ band which—with weak intensity—increases until at $(1/4, 3/4)$ it reaches the top of the blue ZY' ridge where the $|\mathbf{k}$ character takes over and the $xz(\mathbf{k})$ band continues with full intensity downhill. The lower xy band disperses parabolically upward from Λ and reaches the Fermi level half the way to W , and the same is seen—with reduced intensity—along $\Lambda'W'$ ($k_c = 3/4$) for the higher xy band. The nonvanishing hopping integrals I (46) between an xy WO and an xz or yz WO causes the corresponding bands to repel where they run close. This is the case for the two xy bands and the $yz(\mathbf{k})$ band between Λ and $(1/4, 1/4)$, and for the two xy bands and the $xz(\mathbf{k})$ band between Λ' and $(1/4, 3/4)$. It is remarkable that of the three close bands, *two* repel around the third band, which remains unaffected and thereby ends up as the band of intermediate energy, the lowest of the two xy bands

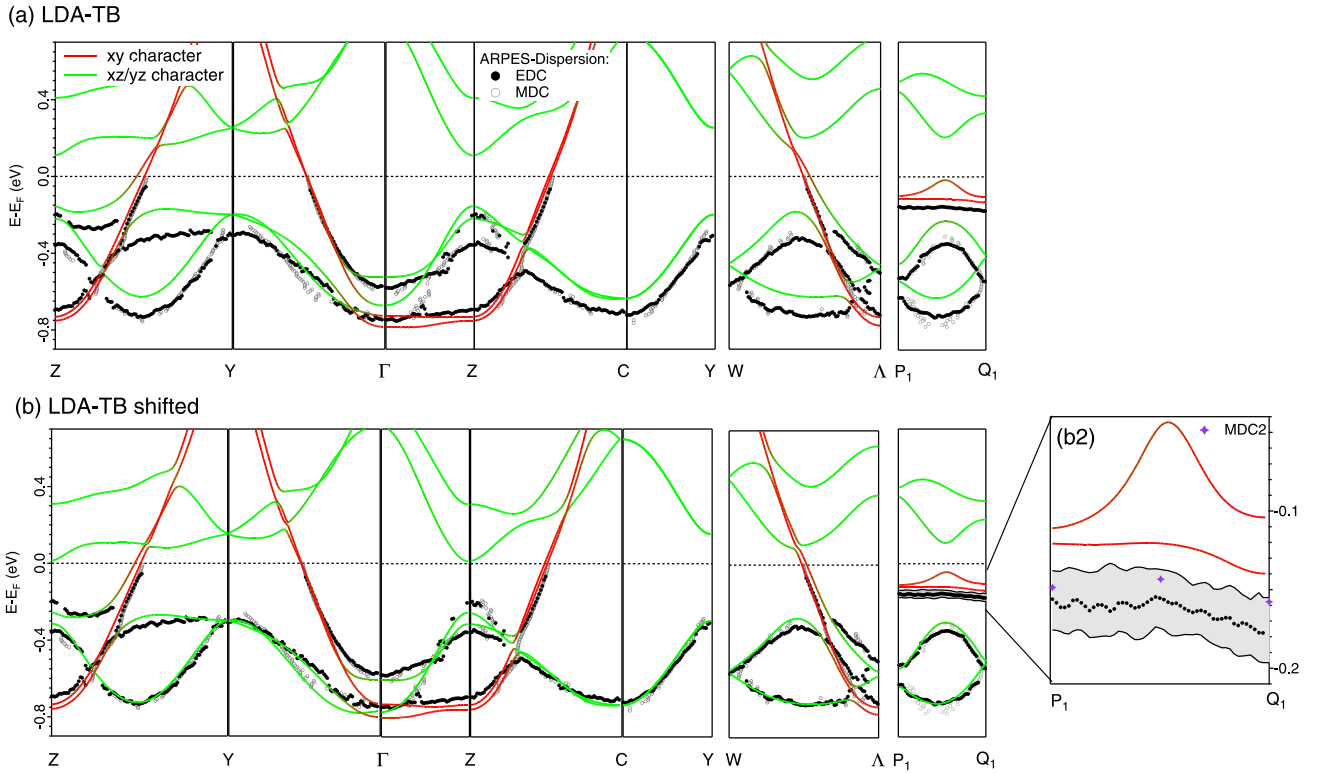


FIG. 12. ARPES (black dots and gray circles) and LDA (xy red, xz and yz green) band structures. The line P_1Q_1 has $k_b = 0.225$ and $k_c = 0$ to 0.5, see Figs. 1, 10, and 11(a). The experimental bands come from the *symmetrized* ARPES measurements ($T = 6K$, $h\nu = 30$ eV) on sample H whose metallic bands are 51% filled (see Sec. III B 1 in paper III [2]) and displayed in Fig. 11(c). They were determined by searching the intensity maximum along the direction of either energy (EDC, black dots) or momentum (MDC, gray circles). (a) The LDA bands are the eigenvalues of the six-band TB Hamiltonian defined in Sec. I VI with the parameters listed in Tables I (43)–I (47) and I (49). (b) As above, but with the energy of the xy WOs shifted 100 meV upwards. The blow-up along P_1Q_1 in panel (b2) compares the shifted LDA-TB theory with the experimental band (black dots with uncertainty in gray). The diamonds, labeled “MDC2,” indicate the band determined from the maximum along the momentum direction \mathbf{b}^* perpendicular to P_1Q_1 , where the band disperses strongly.

in the present case. This can be seen in Figs. 11(c)–11(e) and will be referred to often in the following.

The $P_1Q_1P'_1$ line ($k_b = 0.225$) is perpendicular to the ΛW and $\Lambda'W'$ lines and is parallel to but slightly inside the FS so that the trace of the xy bands is ≈ 170 meV below the Fermi level and thereby clearly visible in ARPES—albeit with the usual xy form-factor reduction of the intensity toward P'_1 . Starting from P_1 , we see the blue $xz(\mathbf{k})$ band reaching its bottom midway to Q_1 and—above it, with slightly less intensity,—the green $yz(\mathbf{k})$ band rising toward the top of the green ridge where 50% of its character and intensity are lost and losing even more on the downhill side toward Q_1 . Proceeding from here toward P'_1 in the second green zone, we vaguely see the green yz band—now $|\mathbf{k} + \mathbf{c}^*$)-like—reach its bottom midway to P'_1 . From Q_1 in the blue first zone, we see the blue xz band rise to the ZY' ridge, where it—like the green yz band at the green ridge—has lost half its intensity and thereafter vanish on the downhill side toward P'_1 . All of this agrees with the $|\mathbf{k}$ characters of the four lowest LDA-TB bands shown at the bottom of Fig. 4 and, at the top, with the xy form factor dropping in the second BZ, thus hiding the resonance peak predicted to exist in the upper $\tilde{x}\tilde{y}$ band.

Before attempting to extract ARPES data beyond the 100 meV scale, we need to assess the degree of agreement between the LDA and the ARPES dispersions.

IV. AGREEMENT BETWEEN ARPES AND THE LOCAL DENSITY APPROXIMATION

The band structure derived from the symmetrized ARPES data is shown in Figs. 12(a) and 12(b). The points indicated by gray circles were extracted from the peak locations in the momentum distribution curves (MDCs), $I(|\mathbf{k}|$ in a specified direction, fixed energy E), and the points indicated by black dots were extracted from peak locations in energy distribution curves (EDCs), I (fixed \mathbf{k} , E). The peak maxima in these curves were found from the zeros in the smoothed first derivative with respect to $|\mathbf{k}|$ for an MDC, or E for an EDC, under the condition that the smoothed second derivative is smaller than zero.

The bands resulting from the first-principles LDA calculation (in the TB representation of the six t_{2g} WOs; see Secs. V and VI in paper I [1]) are shown in 12(a), with the sum of the xz and yz characters in green and the xy character in red. Note the strong hybridization of the nearly degenerate bottoms of the two xy and the xz and yz valence bands near Γ . Note also the hybridizations between Z and Y and between W and Λ . Near the middle of the latter line where the two degenerate xy bands in the gap come close to the valence and conduction (V and C) bands, and their repulsion is therefore strong—but in opposite directions—one of the xy states stays unaffected

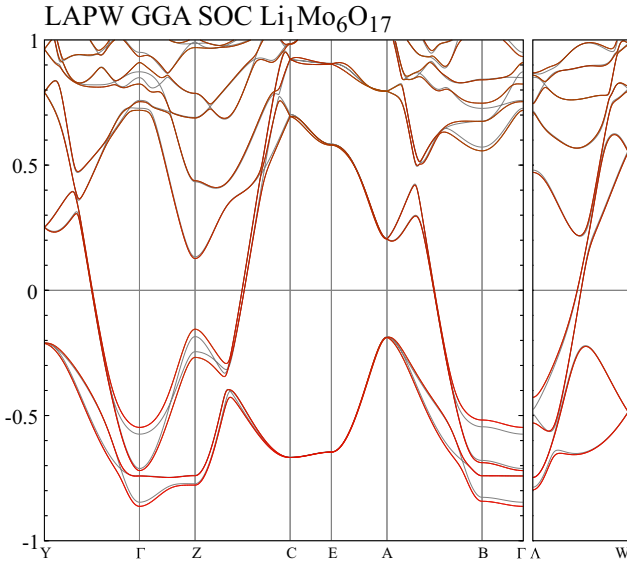


FIG. 13. Relativistic linearized augmented plane wave generalized gradient approximation (LAPW GGA) control calculation of the LiPB band structure using the Perdew-Burke-Ernzerhof (PBE) functional [22]. We show the bands along the same lines in the BZ as shown at the top of Fig. 13 whose bottom shows the 336 NMTO LDA band structure. The 6 NMTO TB band structure in the $Y\Gamma ZC$ plane is shown in Fig. 14. LAPW band energies are in eV with respect to E_F . Red bands are with and gray bands are without spin-orbit coupling. We see that the crossings between the third and fourth bands along ΓZ and ZC and between the first and second bands between $Y\Gamma$ and AB are spin-orbit split by about 80 meV.

and the other is pushed up or down in energy, depending on whether the repulsion from the valence or the conduction band is stronger. Since this balance tips as we move up through the gap, the hybridization shifts from the upper to the lower xy band and causes the resonance peak to shift from upwards pointing in the upper band, to downwards pointing in the lower band. The fact that the matrix element $\alpha(\mathbf{k}) + a(\mathbf{k})$ for hybridization of the xy and xz/yz bands decreases with increasing k_b causes the rather strange-looking dispersion of the two xy bands along ΛW . This asymmetry will be explained in Sec. II B 5 in paper III [2]. Along P_1Q_1 , we clearly see the resonance peak in the upper \tilde{xy} band.

A. Shifting the local density approximation xz and yz bands downwards with respect to the xy bands

Overall in Fig. 12(a), there is good agreement with the occupied ARPES bands, the main discrepancy being that the LDA valence bands lie 100 meV too high with respect to the xy bands and therefore with respect to the Fermi level. This may be partly a surface effect: The xz and yz WOs reach farther into the vacuum and therefore feel a higher LDA potential than the xy WOs which are well inside the staircase. In addition, there is undoubtedly an LDA error; for instance, LDA band gaps in semiconductors are too small, and FS measurements for bulk 4d metals indicate that the accuracy with which the LDA describes the energy separation

between inequivalent t_{2g} levels is ≈ 50 meV.⁹ For LiPB, we therefore correct the bulk LDA bands by shifting the energy of the green V and C bands downwards by 100 meV [more precisely, we shift the on-site energy τ_0 of the xy and XY WOs 100 meV upwards, i.e., from 47 to 147 meV in Eq. I (43) with respect to the common on-site energy of the xz , XZ , yz , and YZ WOs, and subsequently recalculate the Fermi level]. The result shown in 12(b) agrees very well with ARPES, as was seen already in Fig. 10(b) for the CECs. An exception is near Z, where the splitting of the valence band is too small and the lowest conduction band nearly touches the Fermi level, thus asking for a fine adjustment of the TB parameters.

The LDA and ARPES band structures in Figs. 12(a) and 12(b) are lined up with respect to the Fermi level, which for the LDA calculation for stoichiometric $\text{LiMo}_6\text{O}_{17}$ corresponds to 50% filling of the metallic bands. In the experiment, Li and O vacancies make the filling uncertain and is estimated from the measured k_{Fb} value (Sec. III B in paper III) to be $51 \pm 1\%$, i.e., to have the effective stoichiometry $\text{Li}_{1.02 \pm 0.02}$. Using the measured Fermi-velocity, this then gives a Fermi level which with respect to the band structure is between 50 and 0 meV above the level for the stoichiometric crystal assumed in the calculation, which means that the metallic ARPES bands could lie 50 to 0 meV below the LDA bands in Fig. 12(b). But this can only account for the ≈ 40 meV distance to the lower LDA \tilde{xy} band seen in a direction perpendicular to \mathbf{b}^* , such as along P_1Q_1 , in particular in the blowup in Fig. 12(b2).

The black dots in Fig. 12(b2) were obtained as the position of the EDC maxima (*one* for each \mathbf{k}) and the gray area indicates the uncertainty of the experiment, as well as the uncertainty in determining the position of the one EDC maximum. The three purple diamonds labeled MDC2 are from MDCs along, respectively, ΓY , ΛW , and ZC , perpendicular to P_1Q_1 .

The upper \tilde{xy} band predicted by the LDA seems to be missing in the symmetrized ARPES data of Fig. 12(b2). This we can understand by going back to the ARPES bands “as-measured” along $P_1Q_1P'_1$ in Figs. 11(d) and 11(e), where intensity just below the Fermi level was seen in the first BZ but hardly in the second BZ. As illustrated in Fig. 4, the lower xy band is selected in the first and the upper band in the second BZ. Since for $k_b = 0.225$, the xy bands are closer to the valence than to the conduction bands, the repulsion from the former dominates and pushes a resonance peak *up* in the *upper* band. This peak thus has ARPES intensity in the second zone where it gets strongly reduced by the xy form factor. The symmetrization of the P_1Q_1 and $Q_1P'_1$ ARPES data finally adds to hiding the band in the second BZ behind the one seen in the first BZ, and that is why, in Fig. 12(b2), only the lower ARPES band is seen. From the ARPES data, we can therefore only uncover the upper \tilde{xy} band if we *avoid* the symmetrization.

⁹For elemental transition metals, 100 meV is the typical size of the s -to- d energy shift needed to bring the LDA and experimental (de Haas-van Alphen) Fermi surfaces into agreement, see Ref. [23].

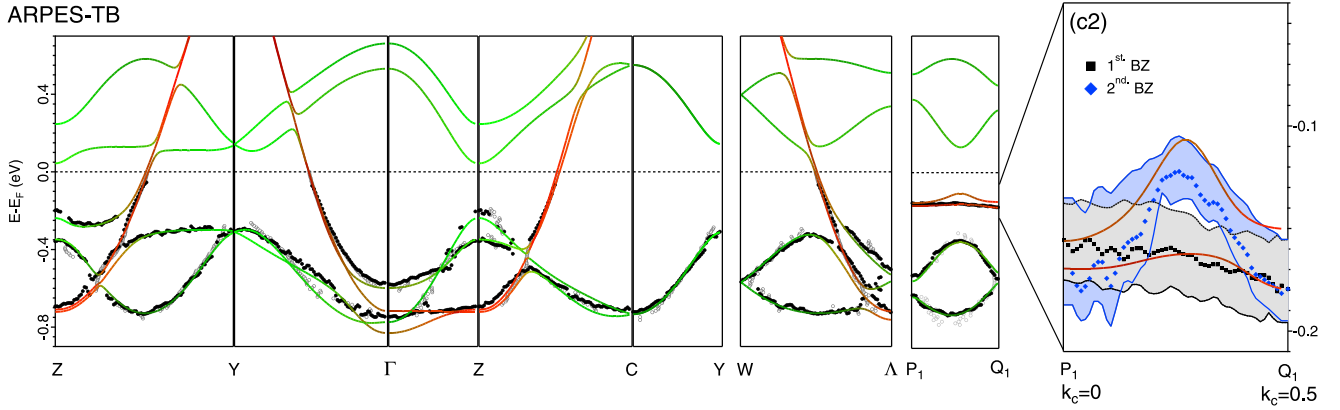


FIG. 14. Band structure obtained as the eigenvalues of the six-band TB Hamiltonian, Eqs. I (35) or I (56), with parameter values fine-tuned to improve the fit to the ARPES bands and given in the square parentheses in Eqs. I (43)–I (47). The Fermi level is ≈ 0.1 eV above the center of the gap [see text following Eq. I (49)]. The ARPES data here are those already shown in Fig. 12, except for those in the blowup (c2) along P_1Q_1 ($k_b = 0.225$), which are *non-symmetrized* EDC data from, respectively, the first (black) and second (blue) BZ. The latter data are subsequently mirrored around the $k_c = 0.5$ zone boundary into the first BZ.

B. Fine tuning the tight-binding Hamiltonian and extracting both quasi-one-dimensional bands from ARPES as measured

Our first-principles LDA TB description of the six lowest energy bands given in Sec. I VI has about 40 TB parameters (WO energies and hopping integrals). Their LDA values, derived as described in Sec. I II, are given in Tables I (43)–I (47) and yield the band structure shown in Fig. 12(a). As explained above, the improved agreement with ARPES seen in panel 12(b) was achieved by merely shifting the value of τ_0 , the energy of the degenerate xy and XY WOs, up with respect to that of the degenerate xz , XZ , yz , and YZ WOs. The latter is the energy at the center of the gap and is taken as the zero of energy in the TB Hamiltonian. Still, the Fermi velocity is too small and the resonance peak along P_1Q_1 is too high. Moreover, the levels near Z, where the V and C bands come closest, remain inaccurate: the splitting of the valence-band levels is too small while that of the conduction-band levels is too large. This is due to bad convergence and truncation of the xz - yz hybridizations I (40), to our neglect of the spin-orbit coupling in the NMTO—but not in the linearized augmented plane wave (LAPW) (Fig. 13)—calculation, and to the LDA yielding too small a gap.

We therefore refined the parameter values, with the results given in square parentheses in Tables I (43)–(47). Specifically, we found it necessary to modify the values of the intra-ribbon hopping integrals, first of all, between, respectively, the on-site, first-, and second-nearest xy WOs τ_0 , τ_1 , and τ_2 . This increases the Fermi velocity by about 15%, increases the upward curvature of the bands near half filling, and lowers the half-filling Fermi level to 53 meV above the center of the gap. Second, we refined the values of the xz - yz hopping integrals m_1 , λ_2 , and λ_3 in Table I (47). In addition, the value of the gap parameter G_1 originating in the asymmetry (dimerization) between the forward and backward hoppings, $xz \leftrightarrow XZ$ ($yx \leftrightarrow YZ$), as explained after Eq. I (27) and given in Eq. I (45), was increased by 10%. The resulting band structure is displayed in Fig. 14 and is seen to agree almost perfectly with the experiment.

Most importantly, we have succeeded in extracting *both* metallic bands by using the ARPES data *as measured* along $P_1Q_1P'_1$ ($k_b = 0.225$) for the EDCs. These ARPES bands are displayed in the blowup of Fig. 14(c2) where the band obtained in the first zone from P_1 to Q_1 has been plotted in black squares with the uncertainty in gray, and the band obtained in the second zone from Q_1 to P'_1 has been plotted in reverse order, from Q_1 to P'_1 in the first zone, and in blue. Even though the second BZ emission is relatively weak in this $h\nu = 30$ eV data (recall from Sec. III C 2), nonetheless, we now see at midzone the resonance peak in the blue upper band, well separated from the gray lower band, while near $k_c = 0, 0.5$, and 1, the splitting of the two bands is less clear. The reasons for the latter are technical:

(1) The extraction was done by assuming only one (possibly broad) maximum per EDC whereby in the zone-boundary (ZB) region ($0.4 < k_c < 0.6$) where both bands have a significant $|\mathbf{k}$ projection, only one band is found (see red bands in the middle and bottom parts of Fig. 4). In Fig. III 8 we see an example of how the one-peak extraction method switches between the two bands when the ZB is crossed.

(2) With the ARPES intensity fading away upon approaching $k_c = 1$ (P'_1), smoothing the EDCs before taking the derivative (to locate the maximum) pushes the intensity to increasingly higher binding energies ω and thereby causes the band near P'_1 , which is the (blue) upper band, to fall below the one near P_1 , which is the (gray) lower band.¹⁰

Figure 14 thus demonstrates that the refinement of merely seven out of the more than 40 TB parameters to fit the ARPES bands, lying more than 0.15 eV below the Fermi level, achieves nearly perfect agreement *also* for the k_c dispersion of the quasi-1D bands closer to the Fermi level. This includes agreement with the size and shape of the resonance peak in the upper band, *without* having modified any of the 17 (a, g, α, γ)

¹⁰The uncertainty of this is not included in the blue uncertainty interval.

parameters I (46) describing hybridization between the xy and the xz and yz bands. This clearly shows the decisive role that resonant coupling to the gapped xz and yz bands plays in determining the splitting and dispersion of the metallic xy bands.

Besides the above-mentioned peculiarities and experimental uncertainties, the agreement between ARPES and the refined TB bands is astonishingly good. In both cases, the peak caused by the resonance with the xz valence band at $(k_b, k_c) = (0.225, 0.725)$ —mirrored around the $k_c = 0.5$ line to the resonance with the yz valence band at $(0.225, 0.275)$ —comes out clearly in the upper \tilde{xy} band, and so does the *lack* of a visible resonance peak in the *lower* band at $(0.225, 0.275)$.

C. True value of the fine-tuning fit

While it is intrinsically very satisfying to obtain a good fit to the ARPES data, the true value of the fit is the very fact that it was possible to do. Thus we know that our analytic TB representation of the bands, as inferred from the LDA results, is fundamentally correct at the qualitative level, and is not missing any essential underlying physics. Otherwise, merely varying the magnitudes of parameters could not achieve a good fit. In particular, as emphasized already, obtaining a good description of the low-energy FS features by fitting only the high-energy features serves to validate our essential insight that the details of these FS features do indeed result from their couplings to the higher-energy valence and conduction bands.

Therefore we proceed to use the refined TB model in the following paper III to focus on the metallic \tilde{xy} bands in the gap, the origins of their observed k_c dispersion on the 10 meV scale, and their k_c dispersion as a function of their position in the gap, i.e., of the k_b value. This will enable us to study the details of the FS. We see that the theoretical splitting between the two metallic bands near the $|k_c| = 0.5$ zone boundary increases as the energy moves away from the valence band and toward the conduction band. With the $h\nu = 33$ eV data (see Fig. 9) the zone-selection rule, and a detailed analysis of our high-resolution data, we shall be able also with ARPES to separate the two FS sheets.

V. SUMMARY AND OUTLOOK

In Sec. II of this paper II we derived a one-electron theory of the ARPES intensity variations in LiPB, which was then used in Sec. III to understand and analyze the extensive data presented there.

For the intensity of photoemission with momentum $\boldsymbol{\kappa}$ and binding energy ω (≥ 0), we used the one-step expression (1) with the least specific choice, plane waves $e^{2\pi i \boldsymbol{\kappa} \cdot \mathbf{r}}$, for the final states, and approximation (2) for the matrix element. As a basis for the initial states, we used the six t_{2g} WOs, $w_m(\mathbf{r})$ and $W_m(\mathbf{r})$, centered on, respectively Mo1 and MO1, the most central molybdenums of the lower and the upper strings, $\text{Mo2} \setminus \text{Mo1} / \text{Mo4} \setminus \text{Mo5}$ and $\text{MO5} \setminus \text{MO4} / \text{MO1} \setminus \text{MO2}$, shown in Fig. I 2(a). Due to the approximate translational equivalence [see Eqs. I (17) and I (18)] of $w_m(\mathbf{r})$ and $W_m(\mathbf{r})$, the photoemission intensity is essentially the projection of the initial-state band with energy $E(\mathbf{k}) = E_F - \omega$ onto the *pseudo* Bloch sum $|w; \mathbf{k}$ in Eq. I (52) with $\mathbf{k} = \boldsymbol{\kappa} - \mathbf{G}$ in the

double zone [see Figs. 1 and 4 (bottom)]. This would have been the initial-state band had the vector distance between Mo1 and MO1 been $(\mathbf{c} + \mathbf{b})/2$ rather than $(\mathbf{c} + \mathbf{b})/2 - \mathbf{d}$, and had $W(\mathbf{r})$ been equal to $w(\mathbf{r})$ rather than inverted around $(\mathbf{c} + \mathbf{b})/2 - \mathbf{d}$. For a band with dominant m character, we thus expected that ARPES will see the lower band if $\boldsymbol{\kappa}$ is in the first physical zone, and the upper band if $\boldsymbol{\kappa}$ is in the second physical zone and the band is occupied. Specifically, that the relative intensity of emission from the upper (lower) m band is $\frac{1}{2}[1 \mp \cos \phi]$, where $\phi_m(\mathbf{k})$ is given by the m -band structure in Eq. I (60). Taking now the c -axis dimerization into account, we found that this expression is modified to $\frac{1}{2}[1 \mp \cos(\phi - \eta)]$, where $\eta_m(\boldsymbol{\kappa}) \equiv 2 \arg \tilde{w}_m(\boldsymbol{\kappa}) - 2\pi \boldsymbol{\kappa} \cdot \mathbf{d}$ is the difference between the phase shifts due to the inversion and displacement dimerizations. These phase shifts were shown in the first column of Figs. 2 and 3 for, respectively, the xy and yz bands. Whereas the inversion phase shift depends more strongly on $\boldsymbol{\kappa}$ for the yz WO than for the more structurally protected xy WO, the displacement phase shift is independent of m and rather constant. We had therefore expected the selection rule to hold better for the xy bands. However, in both cases and with κ_a (which does not influence the band structure) suitably chosen via the photon energy, the inversion and displacement phase shifts tend to cancel with the result that the selection rule holds surprisingly well, provided that κ_a is properly chosen. This was seen in the second column of Figs. 2 and 3.

On top of this fine-grained structure of the photoemission intensity, there is a coarse-grained aperiodic structure given by the WO *form factor* $|\tilde{w}_m(\boldsymbol{\kappa})|^2$. Since in real space the t_{2g} WO (Fig. I 9) spreads with the same m character onto the four to five nearest Mo sites in its plane and on the simple cubic xyz lattice I (12) with 1 Mo per cell, its FT (11) factorizes approximately into a *structure factor* $S_m(\boldsymbol{\kappa})$ times the FT of the “atomic” part of the t_{2g} orbital, factorizing into an angular and a radial part. As explained in Sec. II B 2, the structure factors $|S_{xy}|^2$, $|S_{yz}|^2$, and $|S_{xz}|^2$ form 2D square lattices of beams running in, respectively, the κ_z , κ_x , and κ_y directions in reciprocal space, thus giving rise to intensity patterns which are roughly six times coarser than the zone-selection patterns. The square lattices formed by the beams from $|\tilde{w}_{xy}(\boldsymbol{\kappa})|^2$ and $|\tilde{w}_{yz}(\boldsymbol{\kappa})|^2$ were shown in column 1 of Fig. 5 and the following columns showed how the angular and radial factors limit the intensities to the extent that only the beams passing through $[\kappa_x, \kappa_y, \kappa_z] = [1, 1, 1]$ should be useful for ARPES investigation of all three WOs. A closer look—and in the crystallographic $(\kappa_a, \kappa_b, \kappa_c)$ space—was given in Fig. 6. The central parts of the three form factors were shown in the top part of Fig. 4 along the line $(\kappa_a, \kappa_b) = (6.4, 0.225)$. As seen in the last columns of Figs. 2 and 3, the narrowness of the form factors ($\Delta\kappa_c \approx 1$) washes out details of the dimerization distortions of the zone selection, except near the suitably chosen values of κ_a .

Our extensive ARPES data confirmed the LDA-based WO theory of the energy bands and the ARPES intensity variations. The agreement between the band structures obtained by ARPES and by the LDA is already good (Fig. 12) and refinement of the LDA-TB parameters can make the fit almost perfect for the large energy features (Fig. 14, main panel). So doing automatically improves the results for the small-energy features such as the resonance peaks in the upper metallic

$\tilde{x}\tilde{y}$ band, which are caused by repulsion from the top of the xz or yz valence bands (Fig. 4, bottom). Taking advantage of the BZ selection rule enabled observation of the upper metallic $\tilde{x}\tilde{y}$ band resonance peak [second-BZ data, Fig. 14(c2)]. Although the resonance peak is quite weak in this ARPES data measured at $h\nu = 30$ eV, we understood this difficulty (Sec. III C 2) to stem from the rapid falloff of the form factor of the $\tilde{x}\tilde{y}$ WO (see Fig. 4, top and Fig. 6, left) when moving away from the center of the beam given by Eq. (18). The latter depends on κ_a which is controlled by $h\nu$ [Fig. 7 and Eq. (27)], causing the intensity distribution along the Fermi surface (FS) to depend sensitively on the photon energy (Fig. 9). To observe both metallic $\tilde{x}\tilde{y}$ bands equally well, we need strong emission in both the first and second BZs, and this occurs only for our $h\nu = 33$ eV data.

Our trust in the t_{2g} Hamiltonian with the refined parameter values has thus been strengthened to the extent that, in the following paper III [2], we shall go on using it together with ARPES data taken at $h\nu = 33$ eV to study the splitting and warping of the FS. Such deviations from one dimensionality,

crucial for the physical properties, are tiny and can in Fig. 10 only be seen in the theoretical bands. Moreover, since these deviations are largely induced by the xz and yz bands, as may be realized by comparing the red with the dark-red bands in Fig. 4, they depend sensitively on the Fermi level's distances from these V and C bands and, hence, on the doping.

The resonance peaks are pushed up/down in the upper/lower $\tilde{x}\tilde{y}$ band by the V (C) band edge, whose character is 50% *mixed* $|\mathbf{k}\rangle$ and $|\mathbf{k} + \mathbf{c}^*\rangle$. It was therefore not obvious to what extent the character of the original xy bands (the red ones in the middle panel of Fig. 4) near $k_c = \pm 0.75$ or ± 0.25 are retained in the $\tilde{x}\tilde{y}$ bands, and, hence, how strong the ARPES intensity, proportional to the $|\mathbf{k}\rangle$ character, should be. We therefore needed to compute the $|\mathbf{k}\rangle$ characters of the $\tilde{x}\tilde{y}$ bands, the dark-red ones in the bottom panel of Fig. 4. This was done using a two-band Hamiltonian obtained by Löwdin downfolding of the V and C blocks of the six-band Hamiltonian I (56) in the $\{|\mathbf{k}, \mathbf{k} + \mathbf{c}^*\rangle\}$ representation. The derivation of this two-band Hamiltonian will be our first task in the following paper III [2].

-
- [1] L. Dudy, J. W. Allen, J. D. Denlinger, J. He, M. Greenblatt, M. W. Haverkort, Y. Nohara, and O. K. Andersen, companion paper, *Phys. Rev. B* **109**, 115143 (2024).
- [2] L. Dudy, J. W. Allen, J. D. Denlinger, J. He, M. Greenblatt, M. W. Haverkort, Y. Nohara, and O. K. Andersen, companion paper, *Phys. Rev. B* **109**, 115145 (2024).
- [3] E. L. Shirley, L. J. Terminello, A. Santoni, and F. J. Himpsel, *Phys. Rev. B* **51**, 13614 (1995).
- [4] S. Moser, *J. Electron Spectrosc. Relat. Phenom.* **214**, 29 (2017).
- [5] F. Matsui, T. Matsushita, and H. Daimon, *J. Electron Spectrosc. Relat. Phenom.* **195**, 347 (2014).
- [6] H. Daimon, S. Imada, H. Nishimoto, and S. Suga, *J. Electron Spectrosc. Relat. Phenom.* **76**, 487 (1995).
- [7] H. Nishimoto, T. Nakatani, T. Matsushita, S. Imada, H. Daimon, and S. Suga, *J. Phys.: Condens. Matter* **8**, 2715 (1996).
- [8] V. Strocov, L. Lev, F. Alarab, P. Constantinou, X. Wang, T. Schmitt, T. Stock, L. Nicolaï, J. Očenášek, and J. Minár, *Nat. Commun.* **14**, 4827 (2023).
- [9] Z.-H. Zhu, C. N. Veenstra, S. Zhdanovich, M. P. Schneider, T. Okuda, K. Miyamoto, S.-Y. Zhu, H. Namatame, M. Taniguchi, M. W. Haverkort *et al.*, *Phys. Rev. Lett.* **112**, 076802 (2014).
- [10] Z.-H. Zhu, C. N. Veenstra, G. Levy, A. Ubaldini, P. Syers, N. P. Butch, J. Paglione, M. W. Haverkort, I. S. Elfimov, and A. Damascelli, *Phys. Rev. Lett.* **110**, 216401 (2013).
- [11] W. McCarroll and M. Greenblatt, *J. Solid State Chem.* **54**, 282 (1984).
- [12] M. L. Knotek and P. J. Feibelman, *Phys. Rev. Lett.* **40**, 964 (1978).
- [13] J. Denlinger, G.-H. Gweon, J. Allen, J. Marcus, and C. Schlenker, *J. Electron Spectrosc. Relat. Phenom.* **101-103**, 805 (1999).
- [14] K. Breuer, D. M. Goldberg, K. E. Smith, M. Greenblatt, and W. McCarroll, *Solid State Commun.* **94**, 601 (1995).
- [15] S. Moser, L. Moreschini, J. Jačimović, O. S. Barišić, H. Berger, A. Magrez, Y. J. Chang, K. S. Kim, A. Bostwick, E. Rotenberg *et al.*, *Phys. Rev. Lett.* **110**, 196403 (2013).
- [16] S. M. Walker, F. Y. Bruno, Z. Wang, A. de la Torre, S. Ricco, A. Tamai, T. K. Kim, M. Hoesch, M. Shi, M. S. Bahramy *et al.*, *Adv. Mater.* **27**, 3894 (2015).
- [17] L. Dudy, M. Sing, P. Scheiderer, J. D. Denlinger, P. Schütz, J. Gabel, M. Buchwald, C. Schlueter, T.-L. Lee, and R. Claessen, *Adv. Mater.* **28**, 7443 (2016).
- [18] L. Dudy, J. D. Denlinger, J. W. Allen, F. Wang, J. He, D. Hitchcock, A. Sekiyama, and S. Suga, *J. Phys.: Condens. Matter* **25**, 014007 (2013).
- [19] F. Wang, J. V. Alvarez, J. W. Allen, S.-K. Mo, J. He, R. Jin, D. Mandrus, and H. Höchst, *Phys. Rev. Lett.* **103**, 136401 (2009).
- [20] S. Hüfner, *Photoelectron Spectroscopy: Principles and Applications* (Springer Science & Business Media, Heidelberg, 2013).
- [21] A. Damascelli, *Phys. Scr.* **T109**, 61 (2004).
- [22] J. P. Perdew, K. Burke, and M. Ernzerhof, *Phys. Rev. Lett.* **77**, 3865 (1996).
- [23] A. Mackintosh and O. K. Andersen, *The Electronic Structure of Transition Metals* (Cambridge University Press, Cambridge, 1980), Chap. Electrons at the Fermi surface, pp. 149–224.